Neurobiology of Disease 227 (2026) 107492

Contents lists available at ScienceDirect

Neurobiology of Disease

journal homepage: www.elsevier.com/locate/ynbdi

Miro1 mutations disrupt cellular calcium homeostasis via dysregulation of mitochondria-ER-contact-sites, rendering iPSC-derived neurons more susceptible to lipid peroxidation

Anna E. Bartalis [a], Jack Genschmar [a], Julia C. Fitzgerald [b], Andreas Hermann [a,c,d,e], Dajana Grossmann [a,*]

[a] Translational Neurodegeneration Section "Albrecht Kossel", Department of Neurology, University Medical Center Rostock, University of Rostock, Gehlsheimer Str. 20, 18147 Rostock, Germany
[b] Department of Neurodegenerative Diseases, Hertie Institute for Clinical Brain Research, University of Tübingen, Otfried Müller Str. 27, 72076 Tübingen, Germany
[c] Center for Transdisciplinary Neurosciences Rostock (CTNR), University Medical Center Rostock, University of Rostock, Gehlsheimer Str. 20, 18147 Rostock, Germany
[d] German Center for Neurodegenerative Diseases (DZNE) Rostock/Greifswald, Gehlsheimer Str. 20, 18147 Rostock, Germany
[e] United Neuroscience Campus Lund-Rostock (UNC), Rostock site, Gehlsheimer Str. 20, 18147 Rostock, Germany

ARTICLE INFO

Keywords:
Miro1
Calcium
MERCS
Lipid peroxidation
Ferroptosis
Parkinson's disease

ABSTRACT

The pathogenesis of Parkinson's disease is multifactorial, but disruption of calcium and iron is a common feature. The mitochondrial Rho GTPase Miro1 is a component of the mitochondrial–endoplasmic reticulum contact sites and a key regulator of calcium homeostasis. Heterozygous variants in the Miro1-encoding gene *RHOT1* were identified in Parkinson's disease patients. Neurons harboring Parkinson's disease-associated variants show defects in mitochondrial calcium regulation and mitochondria-ER contact sites organization which we hypothesize to contribute to neuronal vulnerability. However, the exact mechanism is not fully understood. We systematically assessed the role of Miro1 and its different domains by using a set of isogenic lines with gene edited mutations S156A and K572R in PINK1/Parkin regulatory elements and the Parkinson's disease-associated mutation R272Q. This showed us a general role of Miro1 in the regulation of cellular calcium homeostasis and the regulation of mitochondrial–ER contact sites, but more importantly, a domain-specific involvement of local calcium distribution, impaired store operated calcium entry and vulnerability to ferroptosis. These findings indicate that Miro1-mutant specific impairments in cellular calcium handling contributes to neuronal vulnerability via mitochondria-ER contact sites and provides further insights in the mechanism how impaired regulation of Miro1 impacts neurons in the context of Parkinson's disease.

1. Introduction

Parkinson's disease (PD) is characterized by the progressive loss of dopaminergic neurons in the substantia nigra pars compacta and the accumulation of Lewy bodies (Spillantini et al., 1997; Forno, 1996). Although the precise mechanisms underlying these pathological changes remain unclear, numerous PD-associated genes have been implicated in the regulation of mitochondrial quality control and function (Klein and Westenberger, 2012). Beyond their role in energy production, mitochondria are key regulators of calcium homeostasis, which is commonly disrupted in PD (Ludtmann and Abramov, 2018; Chan et al., 2009). Particularly, the specialized regions of mitochondria–endoplasmic reticulum contact sites (MERCS) and their function involving calcium homeostasis, lipid exchange, mitochondrial dynamics and autophagy where shown to be disrupted in PD (Lim et al., 2021; Grossmann et al., 2023; Smolders and van Broeckhoven, 2020; Barazzuol et al., 2020; Valadas et al., 2018).

A central player in these pathways is the mitochondrial Rho GTPase Miro1, encoded by the *RHOT1* gene. Miro1 contains a N-terminal GTPase domain, followed by two calcium-binding EF-hand domains, a C-terminal GTPase domain and a C-terminal transmembrane domain that anchors the protein to the outer mitochondrial membrane (Fransson et al., 2006; Klosowiak et al., 2013).

Functionally, Miro1 mediates calcium-dependent mitochondrial

* Corresponding author.
E-mail addresses: Anna.bartalis@med.uni-rostock.de (A.E. Bartalis), Jack.genschmar@uni-rostock.de (J. Genschmar), Julia.fitzgerald@uni-tuebingen.de (J.C. Fitzgerald), Andreas.hermann@med.uni-rostock.de (A. Hermann), Dajana.grossmann@med.uni-rostock.de (D. Grossmann).

https://doi.org/10.1016/j.nbd.2026.107492
Received 8 May 2026; Received in revised form 20 May 2026; Accepted 17 June 2026
Available online 18 June 2026

transport (Chang et al., 2011), and acts as a calcium sensor (MacAskill et al., 2009), processes known to be perturbed in PD (Pozo Devoto and Falzone, 2017). Critically, the PD-associated phosphatase PINK1 and the E3 Ubiquitin ligase Parkin directly target Miro1. Upon phosphorylation and ubiquitination by PINK1/Parkin, Miro1 gets degraded by the proteasome, leading to the arrest of mitochondrial motility and promoting mitophagy of depolarized mitochondria (Hsieh et al., 2016; Wang et al., 2011; Birsa et al., 2014). Recently, Miro1 has emerged as a potential disease marker, supported by abnormal Miro1 retention at damaged mitochondria in sporadic and genetic PD cohorts (Hsieh et al., 2016; Hsieh et al., 2019; Drwesh et al., 2025). Furthermore, variants in *RHOT1* have been reported in PD patients (Grossmann et al., 2019; Berenguer-Escuder et al., 2019). Further evidence is linking Miro1 dysfunction to neurodegeneration especially in PD, as a recent knock-in mouse model expressing Miro1-R285Q, the mouse homolog to human R272Q, led to mitochondrial dysfunction, α-synuclein accumulation and loss of dopaminergic neurons (Chemla et al., 2025).

Together, these findings highlight Miro1 as a central regulator of neuronal health, particularly through its localization at MERCS. At these specialized regions, Miro1 coordinates organelle dynamics (MacAskill et al., 2009) and regulates mitochondrial calcium uptake (Chang et al., 2011; Niescier et al., 2018) and lipid exchange (Guillén-Samander et al., 2021; Endoni et al., 2025), processes essential for cellular homeostasis.

Disruption of calcium homeostasis has previously been linked to cell death via ferroptosis in neuroblastoma cells and rat neurons (Campos et al., 2024; Gleitze et al., 2023) and ferroptosis has been implicated in the pathogenesis of PD by numerous studies, linking impaired calcium homeostasis and neuronal loss (for overview see (Mahoney-Sánchez et al., 2021; Guiney et al., 2017).

To investigate the role of Miro1 in calcium homeostasis and ferroptosis, we examined the R272Q mutation, which was previously identified in a PD patient, and the functional mutations K572R and S156A.

The R272Q mutation affects the first calcium-binding EF-hand domain (Fig. 1A), resulting in impaired cellular calcium handling, alterations in the abundance of MERCS and disturbances in mitophagy in fibroblasts and induced pluripotent stem cell (iPSC)-derived neurons from a PD patient harboring the heterozygous R272Q mutation (Grossmann et al., 2019; Berenguer-Escuder et al., 2020). However, a recent study showed increased reactive oxygen species (ROS) production, elevated cytosolic calcium levels and increased cell death in dopaminergic iPSC-derived neurons with the PD-associated heterozygous R272Q variant, compared to a gene corrected isogenic control (Chemla et al., 2025). An independent isogenic model was generated by introducing the heterozygous R272Q mutation in a healthy iPSC line, revealing alterations in cellular calcium dynamics, disrupted mitochondrial cristae organization, sufficient to disrupt neurotransmitter uptake in dopaminergic neurons (Schwarz et al., 2022).

The S156A mutation compromises the putative PINK1 phosphorylation site (Fig. 1A; Wang et al., 2011; Birsa et al., 2014). Genetic editing of control iPSCs from a healthy donor using CRISPR/Cas9 resulted in the generation of a homozygous Miro1-S156A iPSC line (Schwarz et al., 2021). IPSC-derived neurons revealed that the S156A mutation interfered with the steady state levels of Miro1 and OXPHOS components as well as degradation of mutant Miro1 during mitophagy and impaired mitochondrial respiration and this is dependent on the mitotic or post-mitotic state (Schwarz and Fitzgerald, 2022), although, so far, the Miro1-S156A variant has not yet been studied with regard to its effect on cellular calcium homeostasis.

The K572R mutation renders Miro1 resistant to ubiquitination at K572 by Parkin (Fig. 1A; Klosowiak et al., 2016; Birsa et al., 2014). A heterozygous K572R was introduced into the same iPSC line, generating an isogenic set of Miro1 mutant iPSC (Schwarz et al., 2021). In fact, the group of Walden et al. demonstrated that Miro1 is the preferred substrate for Parkin-mediated ubiquitination and the interaction of Parkin with Miro1 depends on the first EF-hand domain and the C-terminal GTPase domain (Klosowiak et al., 2013). However, the neurons derived from Miro1 K572R iPSCs have not yet been functionally characterized.

Despite Miro1's established role as a calcium-sensing regulator at MERCS, it remains unclear how Miro1 dysfunction affects cellular calcium homeostasis particularly in neurons carrying Miro1 mutations and how this contributes to the loss of neurons. Moreover, the impact of the Miro1 variants on mitochondrial calcium homeostasis has not previously been investigated. Here, we provide evidence that Miro1 mutations lead to altered MERCS dynamics under calcium stress, impaired mitochondrial calcium buffering capacity, alterations in store operated calcium entry (SOCE) and increased susceptibility to lipid peroxidation and ferroptosis, proposing a mechanism that links Miro1 dysfunction to neuronal vulnerability via impaired cellular calcium regulation.

2. Materials and methods

2.1. smNPC cultivation and differentiation into neurons

Small molecule neuronal progenitor cells (smNPC) derived from iPSC with CRISPR/Cas9 engineered mutations in *RHOT1* were previously published and characterized (Schwarz et al., 2021; Schwarz and Fitzgerald, 2022; Schwarz et al., 2022; Table 1).

SmNPC were cultivated in growth medium ((50% DMEM/F12 (ZuL (Life Tech/ Fischer Scientific), 21331-020), 50% Neurobasalmedium (ZuL (Life Tech/ Fischer Scientific), 21103-049), 0.5% N2 (Thermo Fischer Scientific, 17502-048), 1% SM1 (Stemcell Technologies, 05731), 1% Penicillin/streptomycin/Glutamin (Gibco, 10378-016), 3 μM CHIR99021 (Peprotech, 2520691-10MG), 150 μM ascorbic acid (Sigma, A-4544) and 0,5 μM phorbol-12-myristate-13-acetate (PMA; Cayman, 10009634)), on matrigel (Corning, 354234) coated wells. SmNPC were splited using Accutase (Sigma-Aldrich, A6964-500 mL). Cells were regularly tested for mycoplasma (Promo Cell, PK-CA91-1096).

Further differentiation into ventral midbrain neuronal cultures was performed according to a previously established protocol (Reinhardt et al., 2013). SmNPCs were seeded on Matrigel and cultivated for 10 days in patterning medium ((50% DMEM/F12 (ZuL (Life Tech/ Fischer Scientific), 21331-020), 50% Neurobasalmedium (ZuL (Life Tech/ Fischer Scientific), 21103-049), 0.5% N2 (Thermo Fischer Scientific, 17502-048), 1% SM1 (Stemcell Technologies, 05731), 1% Penicillin/streptomycin/Glutamin (Gibco, 10378-016), 1 μM PMA, 100 ng/mL FGF8b (PeproTech, 100–25-250UG), 0.2 mM ascorbic acid (Sigma, A-4544)). Then, the medium composition was changed to (50% DMEM/F12 (ZuL (Life Tech/ Fischer Scientific), 21331-020), 50% Neurobasalmedium (ZuL (Life Tech/ Fischer Scientific), 21103-049), 0.5% N2 (Thermo Fischer Scientific, 17502-048), 1% SM1 (Stemcell Technologies, 05731), 1% Penicillin/streptomycin/Glutamin (Gibco, 10378-016), 0.5 μM PMA and 0.2 mM ascorbic acid) for two days. The cells were then transferred to cell culture vessels suitable for the respective experiments, coated with Poly-L-Ornithine (Merck/Sigma-Aldrich, A-004-C) and Laminin (Biotechne, 3400-010-02), and neuronal cultures were cultivated for 14 days in maturation medium (50% DMEM/F12 (ZuL (Life Tech/ Fischer Scientific), 21331-020), 50% Neurobasalmedium (ZuL (Life Tech/ Fischer Scientific), 21103-049), 0.5% N2 (Thermo Fischer Scientific, 17502-048), 1% SM1 (Stemcell Technologies, 05731), 1% Penicillin/streptomycin/Glutamin (Gibco, 10378-016), 500 μM dBcAMP (Hölzel Diagnostik/ BioGems, 1698950), 10 ng/mL BDNF (Fisher Scientific/ Peprotech, 17874523/ 450-02-50UG), 0.2 mM ascorbic acid (Sigma, A-4544), 1 ng/mL TGfβ-3 (Peprotech, 17881443/ 100-21C) and 10 ng/mL GDNF (Thermo Fisher/ Peprotech, 450-10-50UG).

Neuronal cultures were assessed by immunostaining with antibodies against Mikrotubuli-associated protein 2 (MAP2; Abcam ab5392, dilution 1:10000) and Tyrosin Hydroxylase (TH; Pel-Freez P40101, dilution 1:1000).

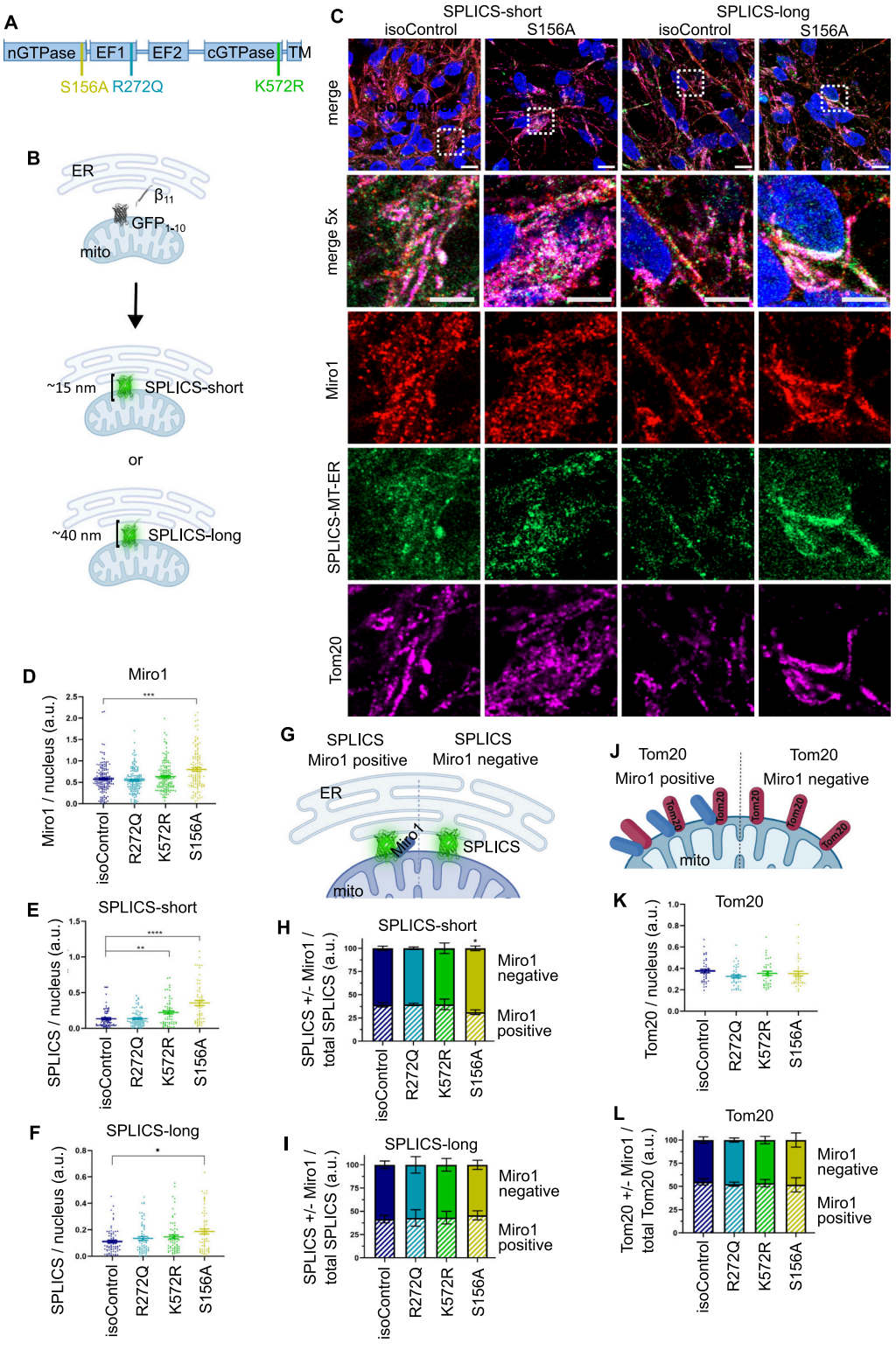

(caption on next page)

Fig. 1. Quantitative analysis of MERCS. A Schematic overview of Miro1 mutations S156A, R272Q and K572R in the Miro1 protein structure. B Schematic representation of the split-GFP construct for narrow and wide MERCS. C Neurons were transfected with either SPLICS-short or SPLICS-long and labeled with antibodies against Miro1 and Tom20. Scale bar indicates 10 μm (overview) or 5 μm (5× magnification). Images were obtained on an inverted LSM900 AxioObserver.Z1 microscope, fitted with a high-resolution Airyscan 2 module, and a 63×/1.4 NA Plan-Apochromat objective (Zeiss). D Quantitative analysis of Miro1 signal area normalized to the area of nuclei. ($N_{Diff} = 8$, $n_{images/Diff} = 10$) E Quantitative analysis of SPLICS-short signal area normalized to the area of nuclei. ($N_{Diff} = 8$, $n_{images/Diff} = 10$) F Quantitative analysis of SPLICS-long signal area normalized to the area of nuclei. ($N_{Diff} = 8$, $n_{images/Diff} = 10$) G Schematic illustration of SPLICS-short or SPLICS-long positive or negative of Miro1 antibody signal. Quantification of H SPLICS-short and I SPLICS-long proportions which are positive or negative of Miro1, in % of total SPLICS signal. ($N_{Diff} = 8$, $n_{images/Diff} = 10$) J Schematic illustration showing Tom20 associated with or without Miro1. K Quantification of Tom20 signal area normalized to nuclei area. ($N_{Diff} = 4$, $n_{images/Diff} = 10$) L Quantification of the proportion of Tom20 signal which is positive or negative of Miro1 signal, in % of total Tom20 signal. ($N_{Diff} = 4$, $n_{images/Diff} = 10$) Data are presented as mean ± SEM; dots represent individual data points. Statistical analysis was assed using Mixed-effect analysis and Kruskal-Wallis test. *$p \leq 0.05$, **$p \leq 0,01$, *** $p \leq 0.001$, **** $p \leq 0.0001$. mito = mitochondrion, ER = endoplasmic reticulum. Schematic images created with *Biorender.com*.

Table 1
Overview of smNPC lines.

smNPC line	Mutation	Original publication
Isogenic control	–	(Schwarz et al., 2021)
Miro1-R272Q	c.815 G > A (heterozygous)	(Schwarz et al., 2021; Schwarz et al., 2022)
Miro1-K572R	c.1714_1716AAA > GGG (heterozygous)	(Schwarz et al., 2021)
Miro1-S156A	c.466 T > G (homozygous)	(Schwarz et al., 2021; Schwarz and Fitzgerald, 2022)

2.2. Live cell imaging of mitochondrial calcium

Neurons were cultivated in 8 well chamber slides (Ibidi, 80806) at 100,000 cells per well. Then, neurons were transfected with 0.5 μg SPLICS-short (Addgene #164108), using Fuse-it-DNA transfection reagent (Beniag GmbH, 60601) according to the manufacturers´ protocol. Six hours post transfection, neurons were treated with 0.1% DMSO or 100 nM BTP2 (Merck, 203890-5MG). Twenty-four hours post transfection, the neurons were stained with 100 nM MitoTracker Deep Red (Cell signaling: 8778) and 1 μM Rhod-2, AM (Thermo-Fisher: R1244) for 30 min at 37 °C to visualize mitochondria and mitochondrial calcium, respectively. Subsequently, neurons were washed once with full maturation medium and incubated for at least 1.5 h prior to imaging without staining, to obtain a better signal-to-noise-ratio. Neurons were stained with 5 μg/mL Hoechst 33342 (Invitrogen, H1399) for 10 min, then washed with full maturation medium prior to imaging. Live-cell imaging was performed in a preheated chamber maintained at 37 °C and 5% CO_2, using an inverted LSM900 AxioObserver.Z1 microscope equipped with a high-resolution Airyscan 2 module, and a 63×/1.4 NA Plan-Apochromat objective (Zeiss). Neurons were initially recorded for two minutes under baseline conditions, with a frame rate of 1 frame/ 10 s. Then, neurons were treated with either 0.1% DMSO, 1 μM thapsigargin (Sigma-Aldrich, T9033-.5MG), a combination of 1 μM thapsigargin and 10 μM Ru360 (Sigma-Aldrich, 557440-500UG), or 5 μM ionomycin (Merck, 407951-1MG) and the recording was continued for an additionally two minutes at a frame rate of 1 frame/ 10 s. Image analysis was carried out using Fiji (Schindelin et al., 2012).

2.3. Immunocytochemistry

Neurons were cultivated in 8 well or 18 well chamber slides (Ibidi, 80806; Cellvis, C18SB-1,5H) at 100,000 or 25,000 cells per well, respectively. Then, neurons were transfected with SPLICS-short (Addgene #164108) or SPLICS-long (Addgene #164107), using Fuse-it-DNA transfection reagent (Beniag GmbH, 60601) according to the manufacturers´ protocol, for 24 h. Then, neurons were fixed in 4% paraformaldehyde (Morphisto GmbH, 11762.05200) for 20 min at 37 °C, then permeabilized with 0.2% Triton X-100 (in DPBS; PAN Biotech, P04-36500) for 10 min and washed three times in Tris-buffered saline (TBS; ROTH, 9090.3) containing 1% Tween 20 (TBS-T; ROTH, 9127.3). Blocking was performed with Pierce™ Protein-Free Blocking Buffer (Thermo Fischer, 37572) for 1 h at room temperature. Then, neurons were labeled with primary antibodies against Miro1 (Sigma, HPA010687, dilution 1:500) and Tom20 (Santa Cruz, sc-17,764, dilution 1:1000). Primary antibodies were diluted in Pierce™ Protein-Free Blocking Buffer and incubated over night at 4 °C. Samples were washed three times with TBS-T for 10 min, then incubated with secondary antibodies goat anti-mouse Alexa Fluor 647 (Invitrogen A21235, dilution 1:5000) and goat anti-rabbit Alexa Fluro 568 (Invitrogen A11036, dilution 1:5000). Finally, the neurons were mounted with DAPI Fluoromount-G Southern Biotech (Biozol, 0100-20). Image acquisition was performed on an inverted LSM900 AxioObserver.Z1 microscope, fitted with a high-resolution Airyscan 2 module, and a 63×/1.4 NA Plan-Apochromat objective (Zeiss). Image analysis was carried out using Fiji (Schindelin et al., 2012).

2.4. Analysis of store-operated calcium entry

Neurons were cultivated in 96-well plates (Sarstedt, Lumox multiwall, 94.612.096) at 35,000 cells per well. For analysis of cytosolic calcium, neurons were stained with the Fluo-4 Direct™ Calcium Assay Kit (Thermo Fisher Scientific, F10471) for 30 min at 37 °C, followed by a wash in full maturation medium to improve signal-to-noise ratio. The plate reader (TECAN, SPARK, 30086376) was pre-warmed to 37 °C. Immediately prior to the measurement, cells were incubated in calcium-free Ringer solution (125 mmol/L NaCl, 5 mmol/L KCl, 1.2 mmol/L $MgSO_4$, 0.5 mmol/L EGTA, 2 mmol/L $Na_2HPO_4{\cdot}2H_2O$, 32 mmol/L HEPES, 5 mmol/L Glucose). Baseline fluorescence of Fluo-4, AM was recorded for 30 s with a frame rate of 1 frame/10 s, followed by application of 25 μL of 1 μM thapsigargin and recording for 130 s with a frame rate of 1 frame/10 s, at $494_{Ex}/516_{Em}$ nm. Subsequently, 100 μL of Ringer solution containing 2 mmol/L $CaCl_2$ was added, and Fluo-4, AM fluorescence intensity was recorded for an additionally two minutes at a frame rate of 1 frame/10 s, using $494_{Ex}/516_{Em}$ nm.

2.5. SDS-PAGE and western blot

Neurons were cultivated in 12 well plates at 500,000 cells per well (Sarstedt, 83.3921). Depending on the protein of interest the pellets were then processed as follows:

To investigate STIM1 the pellet was lysed with radioimmunoprecipitation assay buffer (RIPA; 20 mM Tris–HCl, pH 7.4; 137 mM NaCl; 2 mM Sodium Deoxycholat; 2 mM EDTA; 1% Triton X-100; 10% Gylcerol; 1% sodium dodecyl sulfate, cOmplete EDTA-free protease inhibitor cocktail (ROCHE, 4693159001), PhosSTOP phosphatase inhibitor (ROCHE, 4906837001)), for 30 min on ice. The lysate was mixed with 5× Lämmli buffer (10% SDS, 50% glycerol, 0.25 M Tris-HCl pH 6.8, 0.02% bromophenol blue, and 5% β-mercaptoethanol) and incubated at 95 °C for 5 min.

For Western blot analysis of the proteins MICU1, VDAC or MCU, the cell pellets were lysed with 2× Lämmli buffer (33,3% 6× Lämmli buffer in distilled H_2O, cOmplete EDTA-free protease inhibitor cocktail (ROCHE, 4693159001), PhosSTOP phosphatase inhibitor (ROCHE, 4906837001), 1 M dithiothreitol (Serva, 20710.03)).

For protein separation, the samples were run on 10% polyacrylamide gels and subsequently transferred to nitrocellulose membranes using the Trans-blot turbo transfer system RTA transfer kit (BioRad, 1704270), on a Trans-blot Turbo transfer system (7 min, 25 V; BioRad). Next, membranes were stained with Total protein stain (Revert™ 700 Total Protein Stain, LICOR, 926–11,021). The membranes were blocked in 5% skim milk (ROTH, T145.3, in TBS-T) for one hour at room temperature, on a shaker. The primary antibodies were incubated over night at 4 °C, on a shaker: STIM1 (CellSignaling, 5668S, dilution 1:1000), MCU (proteintech, 26312-1-AP, dilution 1:5000), VDAC (proteintech, 66435-1-lg, dilution 1:5000) or MICU1 (proteintech, 25905-1-AP, dilution 1:1000), in 5% skim milk. Membranes were washed three times for 15 min with TBS-T, then incubated with secondary antibodies in TBS-T for 1.5 h at room temperature, on a shaker: HRP-conjugated goat anti-mouse (Invitrogen, A16017; dilution 1:5000) or HRP-conjugated goat anti-rabbit (Invitrogen, A16035; dilution 5000). Membranes were then washed three times for 15 min with TBS-T and incubated for five minutes with Prime Western-Blot-Detection reagent (Fisher Scientifics/Life Science Cytiva, Cytiva Amersham™ ECL™, 10308449). Antibody signals were imaged on a Li-COR ODYSSEY XF analyzer and subsequently analysed with Empiria software (Li-Cor Biotech).

2.6. Lipid peroxidation assay

Neurons were cultivated in 96-well plates (Sarstedt, Lumox multiwall, 94.612.096) at 35,000 cells per well. Neurons were treated with 750 μM RSL3 (MERCK, SML2234), 10 μM Ru360 (Sigma-Aldrich, 557440), or 0.5 μM Liproxstatin (Lip-1; Sigma, SML1414) for 48 h. Then, neurons were stained with 2 μM Bodipy665/646 (Thermo fisher, B3932) and 5 μg/mL Hoechst 33342 for 10 min. Live-cell imaging was performed in a preheated chamber maintained at 37 °C and 5% CO_2 levels with a LSM900 Axio Observer Z1/7 microscope using a Plan-Apochromat 20×/0.8 M27 objective (Zeiss).

2.7. Ferroptosis assay

Neurons were cultivated in 96-well plates (Sarstedt, Lumox multiwall, 94.612.096) at 35,000 cells per well. Then, neurons were treated with 500 nM, 750 nM or 1000 nM RSL3 and 0.5 μM Lip-1 for 48 h. Then, neurons were stained with AquaBluer (Boca Scientific, 6015, 1:100) for 4 h and 5 μg/mL Hoechst 33342 for 10 min. AquaBluer intensity was measured using a plate-reader (TECAN, SPARK, 30086376) at 37 °C. Hoechst staining was imaged with a LSM900 Axio Observer Z1/7 microscope using a Plan-Apochromat 20×/0.8 M27 objective (Zeiss). The AquaBluer signal intensity was normalized to the total Hoechst area of each well.

2.8. Statistics

Data in the graphs are presented as mean ± standard error of the mean (SEM). Individual data points from individual images or measurements are presented as individual dots. Each experiment was independently repeated at least three times, with each biological replicate defined as separate neuron differentiation (N_{Diff}). During microscopy, at least 10 images were taken per condition for each biological replicate/differentiation ($n_{images/Diff}$). Details on replicates are provided in the figure legends. Data analysis was carried out using GraphPad Prism 8.1.0 (GraphPad Software, San Diego, CA, USA). Details regarding the statistical tests and *p*-values are provided in the figure legends.

3. Results

3.1. K572R and S156A increase the amount of narrow MERCS

Based on published findings reporting alterations in MERCS in fibroblasts or iPSC-derived neurons from a PD patient harboring the heterozygous R272Q mutation in Miro1 (Grossmann et al., 2019; Berenguer-Escuder et al., 2020), our initial objective was to examine MERCS in our isogenic Miro1 model. For this purpose, we transfected iPSC-derived neurons with split-GFP-based contact site sensors (SPLICS) designed to detect either narrow or wide MERCS (Cieri et al., 2018), called SPLICS-short, or SPLICS-long, respectively (Fig. 1B). Neurons were simultaneously immunolabeled with antibodies against Miro1 and Tom20 (Fig. 1C). Image analysis revealed a significant increase in Miro1 signal per cell in neurons carrying the Miro1-S156A mutation, while the Miro1 antibody signal was indistinguishable between isogenic control, Miro1-R272Q and Miro1-K572R (Fig. 1D). Quantitative analysis of the SPLICS signal showed no alterations in Miro1-R272Q neurons, compared to the isogenic control. SPLICS-short were significantly increased in neurons with the Miro1-K572R mutation, while SPLICS-long were not changed. In S156A-mutant neurons, SPLICS-short and SPLICS-long signal area per cell were significantly increased, compared to the isogenic control (Fig. 1E, F).

Recent studies found that Miro1 plays a crucial role in MERCS function (Kornmann et al., 2011; Endoni et al., 2025; Modi et al., 2019; Qin et al., 2020; Lee et al., 2016). Therefore, we seeked to quantify Miro1-positive and -negative MERCS (Fig. 1G). However, the proportion of Miro1 positive and Miro1 negative SPLICS-short to total SPLICS-short signal was indistinguishable between isogenic control, Miro1-R272Q and Miro1-K572R neurons. In contrast, Miro1-S156A neurons showed significantly less Miro1 positive SPLICS-short compared to Miro1 negative SPLICS-short (Fig. 1H). In all neuronal lines the proportions of Miro1 positive and Miro1 negative SPLICS-long signals were not significantly different (Fig. 1I). In summary, our results indicate that the functional Miro1 variants K572R and S156A affect the amount in narrow MERCS, which have previously been implicated in the regulation of calcium homeostasis (Cieri et al., 2018; Giacomello and Pellegrini, 2016). In addition, the S156A variant also had an effect on the amount of wide MERCS, which had previously been linked to mitophagy (Giacomello and Pellegrini, 2016; McLelland et al., 2018).

We next examined the distribution of Miro1 relative to mitochondria by analyzing the spatial correlation of Miro1 and the outer mitochondrial membrane marker Tom20 (Fig. 1J). Of note, the Tom20 signal area per cell was similar in all neuronal lines (Fig. 1K). There were no statistical differences in the Miro1 positive or Miro1 negative Tom20 fractions in all neuronal lines (Fig. 1L). Hence, mutations in Miro1 likely do not affect the localization of Miro1 to mitochondria.

3.2. R272Q and S156A Miro1 mutations interfere with calcium levels at narrow MERCS or in mitochondria

Previous studies focused on the analysis of the buffering capacity of cytosolic calcium in response to ionomycin in iPSC-derived neurons from a PD-patient with the heterozygous R272Q variant compared to independent control neurons (Berenguer-Escuder et al., 2020) or compared to a gene corrected isogenic control (Chemla et al., 2025), or in response to thapsigargin in isogenic neurons with the heterozygous R272Q variant introduced in a healthy background (Schwarz et al., 2022). However, it has not yet been determined how the R272Q mutation affects mitochondrial calcium levels. The K572R and S156A variants have not yet been studied at all with regard to their effects on calcium homeostasis.

First, the neurons were transfected with SPLICS-short, since narrow MERCS are involved in calcium homeostasis (Cieri et al., 2018; Giacomello and Pellegrini, 2016; Patergnani et al., 2011), and subsequently stained with Rhod-2, AM and MitoTracker Deep Red to label mitochondrial calcium and mitochondria, respectively (Fig. 2A). Neurons were also treated with 100 nM BTP2 for 24 h in order to block the calcium release-activated channel (CRAC) ORAI1 to prevent calcium replenishment across the plasma membrane into the ER (Zitt et al., 2004) (Fig. 2B). Using super resolution live cell imaging, we were able to determine calcium levels specifically at narrow MERCS (SPLICS-

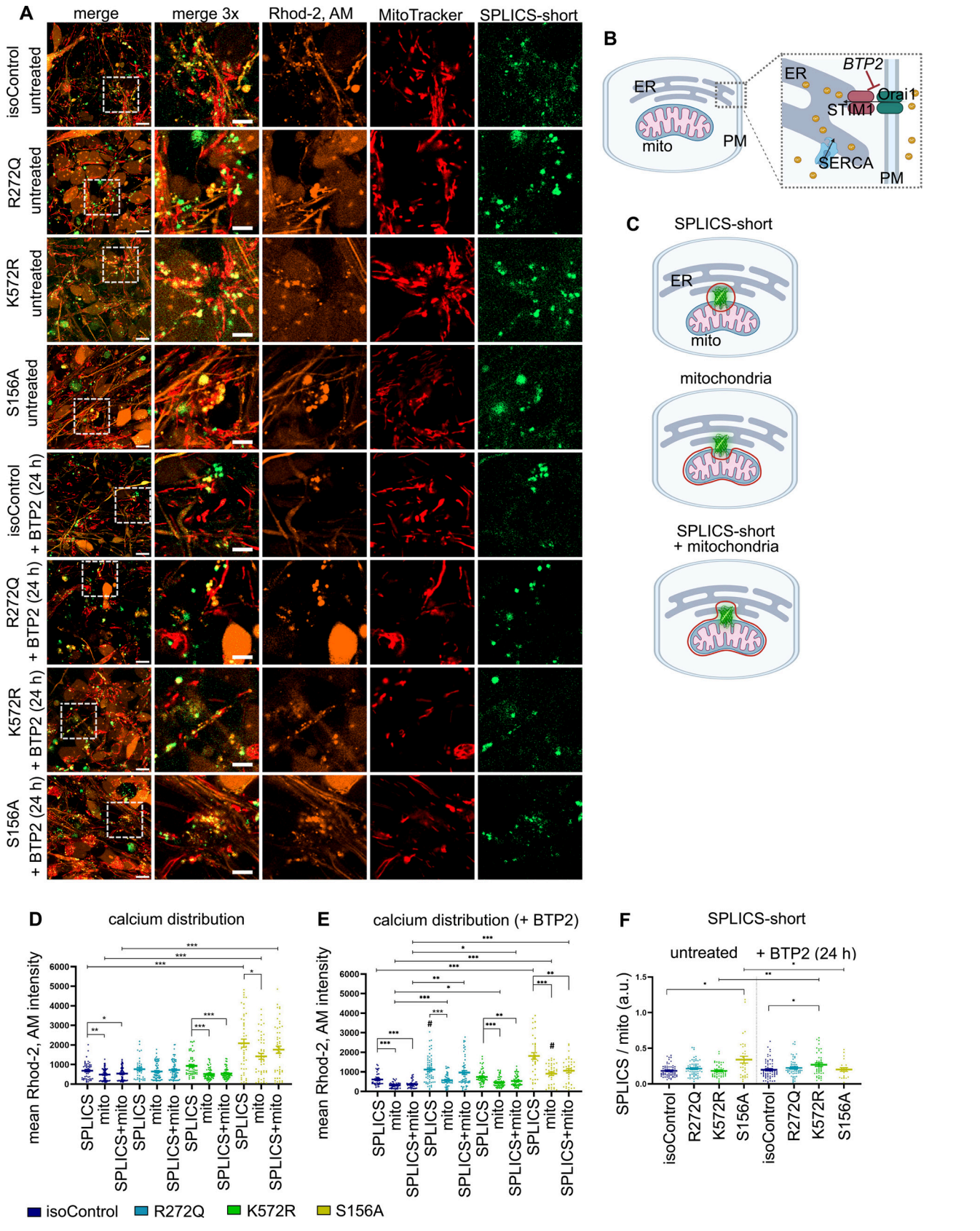

(caption on next page)

Fig. 2. Quantification of mitochondrial calcium levels. A Neurons were transfected with SPLICS-short and subsequently stained with Rhod-2, AM and MitoTracker Deep Red for super-resolution microscopy. Scale bar indicates 10 μm in the overview image or 2 μm in the 3× magnifications. Images were obtained on an inverted LSM900 AxioObserver.Z1 microscope, fitted with a high-resolution Airyscan 2 module, and a 63×/1.4 NA Plan-Apochromat objective (Zeiss). B A part of the neurons were treated with 100 nM BTP2 for 24 h prior to the microscopy in order to inhibit SOCE. C Super resolution live cell imaging enabled us to quantify calcium levels specifically at SPLICS-short labeled narrow MERCS, in mitochondria and at both compartments combined. D Calcium distribution was quantified by Rhod-2, AM intensity in the indicated compartments under baseline conditions. ($N_{Diff} = 7$, $n_{images/Diff} = 10$) E Quantification of calcium levels at SPLICS-short and mitochondria compartments after 24 h of BTP2 treatment. ($N_{Diff} = 6$, $n_{images/Diff} = 10$) F Narrow MERCS were quantified as SPLICS-short signal area normalized to mitochondria area, in untreated neurons and after 24 h of 100 nM BTP2 treatment. ($N_{Diff} = 7$, $n_{images/Diff} = 10$) All data are presented as mean ± SEM. Statistical significance was determined using the Kruskal–Wallis test. */# $p \leq 0.05$, ** $p \leq 0{,}01$, *** $p \leq 0.001$. (*) mark comparison within the graphs for D) or E). (#) mark comparison between E) neurons treated for 24 h with 100 nM BTP2 and D) neurons at baseline conditions. Mito = mitochondrion, ER = endoplasmic reticulum, PM = plasma membrane. Schematic images created with *Biorender.com*. (For interpretation of the references to colour in this figure legend, the reader is referred to the web version of this article.)

short) and in the mitochondrial compartment (Fig. 2C). Quantification of the Rhod-2, AM signal intensity revealed significantly elevated calcium levels at narrow MERCS (i.e. SPLICS-short) compared to the mitochondrial compartment in the isogenic control neurons, in the Miro1-K572R and the -S156A neurons. Notably, this calcium gradient between SPLICS-short and mitochondria was absent in the Miro1-R272Q mutant neurons. Furthermore, calcium levels at SPLICS-short and in mitochondrial compartments were significantly elevated in S156A-Miro1 mutant neurons, compared to the respective compartments of the isogenic control (Fig. 2D).

The isogenic control and Miro1-K572R neurons showed no changes in calcium distribution upon BTP2 treatment (Fig. 2E), compared to the respective untreated conditions (Fig. 2D). In contrast, BTP2 treatment elevated calcium levels at SPLICS-short, thus restoring the calcium gradient between narrow MERCS and mitochondria in Miro1-R272Q neurons. Calcium levels in the mitochondrial compartments of Miro1-R272Q and -K572R neurons were elevated compared to the mitochondrial calcium level in the isogenic control, after treatment with BTP2. Meanwhile, in Miro1-S156A neurons the calcium levels at the combined MERCS+mitochondria compartment significantly decreased under BTP2, compared to the respective untreated condition, but was still significantly elevated compared to isogenic control treated with BTP2 (Fig. 2E).

As mitochondrial calcium homeostasis is regulated at narrow MERCS (Cieri et al., 2018; Patergnani et al., 2011; Giacomello and Pellegrini, 2016) and BTP2 affects the calcium level at MERCS and in mitochondria, we also assessed the effect of BTP2 on narrow MERCS themselves. Following 24 h of BTP2 treatment, the SPLICS-short area per mitochondria area was significantly increased in Miro1-K572R neurons relative to untreated Miro1-K572R neurons and relative to isogenic controls. Meanwhile in Miro1-S156A neurons the increased amount in narrow MERCS was significantly reduced by BTP2 (Fig. 2F).

In summary, specifically the R272Q and the S156A mutations caused distinct alterations in mitochondrial and MERCS calcium levels, suggesting that Miro1 mutations disrupt mitochondrial calcium handling. Importantly, the inhibition of CRAC channel ORAI1 by BTP2 leads to an amelioration of calcium and MERCS phenotypes, suggesting that SOCE plays a critical role in the dysregulation of MERCS-mediated mitochondrial calcium homeostasis in Miro1-mutant neurons.

3.3. *Miro1 mutations impair mitochondrial calcium buffering and calcium-dependent MERCS dynamics*

Given the observed alterations in MERCS organization and mitochondrial calcium levels in Miro1-mutant neurons, we next investigated how these mutations affect the mitochondrial calcium uptake capacity via MERCS. To achieve this, neurons were transfected with the SPLICS-short construct (Cieri et al., 2018) to visualize narrow MERCS, and stained with Rhod-2, AM to detect mitochondrial calcium and MitoTracker Deep Red to label mitochondria. Single neurons were recorded for two minutes at baseline, followed by two minutes of recording after treatment application.

In order to decipher possible phenotypes, cellular calcium handling was challenged using different treatments: i) 1 μM of the SERCA pump inhibitor thapsigargin, which forces mitochondria to buffer calcium at MERCS (Lytton et al., 1991); ii) a combination of 1 μM thapsigargin and 10 μM Ru360, an inhibitor of the mitochondrial calcium uniporter (MCU), thereby preventing mitochondrial calcium uptake (Ying et al., 1991); iii) 5 μM ionomycin, a calcium ionophore that facilitates calcium influx across the plasma membrane and triggers general mitochondrial calcium uptake (Liu and Hermann, 1978); and iv) 100 nM BTP2 for 24 h prior to the experiment in order to compromise SOCE ((Zitt et al., 2004); Fig. 3A). Calcium levels were determined by measuring Rhod-2, AM intensity within mitochondria or at MERCS compartments (Fig. 3B).

As expected from our previous studies (Grossmann et al., 2023; Grossmann et al., 2026), mitochondrial calcium levels increased significantly after acute ionomycin or thapsigargin treatment in the isogenic control, showing the calcium uptake capacity of mitochondria. Concomitant treatment of thapsigargin together with Ru360 prevented the elevation of mitochondrial calcium levels, confirming the MCU as the main channel for mitochondrial calcium uptake. A pretreatment of neurons with BTP2 for 24 h prior to the imaging likewise prevented mitochondrial calcium influx, suggesting that calcium flux from the ER to mitochondria at narrow MERCS depends on SOCE to ensure a sufficient calcium flow from the ER (Fig. 3C). None of these treatments had any effect on calcium levels at narrow MERCS in the isogenic control neurons, indicating that calcium is sufficiently channeled through the MERCS compartment and buffered by mitochondria or other means (Fig. 3D). In order to investigate the effect of calcium stress on the dynamics of narrow MERCS, we quantified the SPLICS-short signal area at baseline and following pharmacological treatments, normalized per mitochondria area. In isogenic control neurons, SPLICS-short area specifically increased after exposure to thapsigargin, but not in response to other treatments, suggesting that specifically calcium flux at MERCS and calcium uptake into the mitochondria provokes a reorganization of narrow MERCS (Fig. 3E).

In Miro1-R272Q neurons, only the application of ionomycin triggered a significant elevation of mitochondrial calcium levels, while thapsigargin did not show a significant effect (Fig. 3F). These results suggest that mitochondria are in general able to buffer calcium when the cytosolic calcium levels reach a certain threshold, but thapsigargin-induced calcium release from the ER does not seem to be sufficient, maybe due to the observed lack of calcium gradient between the MERCS and the mitochondrial compartment (Fig. 2D).

In Miro1-K572R and -S156A neurons, none of the applied treatments resulted in a significant increase in mitochondrial calcium levels (Fig. 3I, L).

All three Miro1 mutant neuronal lines exhibited higher variability of calcium levels at narrow MERCS specifically upon treatment with ionomycin, and in case of the Miro1-R272Q neurons also after thapsigargin treatment, yet due to the variability not reaching statistical significance (Fig. 3G, J, M). Likewise, the SPLICS-short signal area per mitochondria showed an irregular response pattern to different treatments in all Miro1-mutant neuron lines, hence not reaching statistical significance (Fig. 3H, K, N).

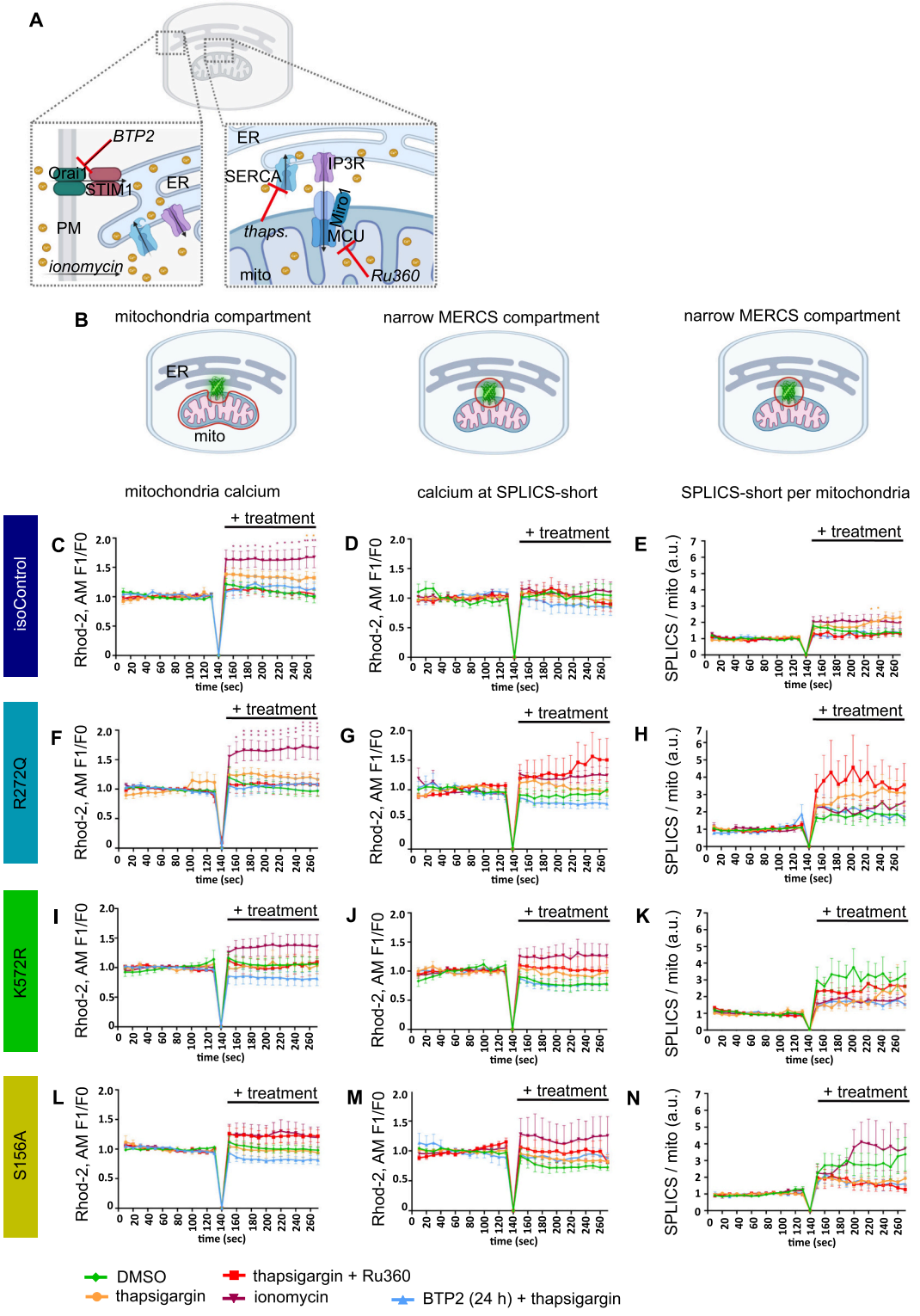

(caption on next page)

Fig. 3. Mitochondrial calcium uptake capacity.
A Schematic illustration indicates the treatments used for the analysis of mitochondrial calcium uptake capacity. A part of the neurons were treated with 100 nM for 24 h prior to the image acquisition in order to inhibit SOCE via ORAI1. Neurons were recorded with super-resolution microscopy for 2 min under baseline conditions, followed by administration of treatments and additional 2 min recording, at a 10 s interval. Videos were obtained on an inverted LSM900 AxioObserver.Z1 microscope, fitted with a high-resolution Airyscan 2 module, and a 63×/1.4 NA Plan-Apochromat objective (Zeiss). Ionomycin facilitates calcium influx across the plasma membrane (PM). Thapsigargin inhibits SERCA at the ER. Ru360 is an inhibitor of the MCU.
B Calcium levels were assessed in the mitochondrial compartment and at SPLICS-short labeled narrow MERCS. Mito = mitochondrion, ER = endoplasmic reticulum, PM = plasma membrane. Schematic images created with *Biorender.com*.
C Quantitative analysis of the mean Rhod-2, AM intensity, normalized to the mean baseline intensity, in mitochondria of isogenic control. ($N_{Diff} = 9$, $n_{videos/Diff} = 1$). Data are presented as mean ± SEM. Two-way ANOVA followed by Dunnett's multiple comparisons test revealed significant effects of treatments [$F(4, 34) = 7.469$; $p = 0.0002$] and significant variation between treatments [$F(34, 408) = 121.3$; $p < 0.0001$]. Multiple comparisons: * $p \leq 0.05$, ** $p \leq 0{,}01$.
D Quantification of the mean Rhod-2, AM intensity, normalized per mean baseline intensity, at SPLICS-short of isogenic control. ($N_{Diff} = 9$, $n_{videos/Diff} = 1$). Data are presented as mean ± SEM. Two-way ANOVA followed by Dunnett's multiple comparisons test revealed significant variation between treatments [$F(37, 444) = 78.19$; $p < 0.0001$]. Multiple comparisons: n.s.
E Quantification of the SPLICS-short signal area normalized to the mitochondria area, normalized to the mean baseline SPLICS-short signal area in isogenic control. ($N_{Diff} = 9$, $n_{videos/Diff} = 1$). Data are presented as mean ± SEM. Two-way ANOVA followed by Dunnett's multiple comparisons test revealed significant interaction between timepoints and treatments [$F(48, 480) = 1.559$; $p = 0.0120$] and significant variation between treatments [$F(40, 480) = 48.50$; $p < 0.0001$]. Multiple comparisons: * $p \leq 0.05$.
F Quantitative analysis of the mean Rhod-2, AM intensity, normalized to the mean baseline intensity, in mitochondria of Miro1-R272Q. ($N_{Diff} = 10$, $n_{videos/Diff} = 1$). Data are presented as mean ± SEM. Two-way ANOVA followed by Dunnett's multiple comparisons test revealed significant effects of treatments [$F(4, 558) = 47.11$; $p < 0.0001$]. Multiple comparisons: * $p \leq 0.05$, ** $p \leq 0{,}01$, *** $p \leq 0.001$.
G Quantification of the mean Rhod-2, AM intensity, normalized per mean baseline intensity, at SPLICS-short of Miro1-R272Q. ($N_{Diff} = 10$, $n_{videos/Diff} = 1$). Data are presented as mean ± SEM. Two-way ANOVA followed by Dunnett's multiple comparisons test revealed significant variation between treatments [$F(42, 504) = 64.35$; $p < 0.0001$]. Multiple comparisons: n.s.
H Quantification of the SPLICS-short signal area normalized to the mitochondria area, normalized to the mean baseline SPLICS-short signal area in Miro1-R272Q. ($N_{Diff} = 10$, $n_{videos/Diff} = 1$). Data are presented as mean ± SEM. Two-way ANOVA followed by Dunnett's multiple comparisons test revealed significant effect of treatments [$F(5, 598) = 10.48$; $p < 0.0001$]. Multiple comparisons: n.s.
I Quantitative analysis of the mean Rhod-2, AM intensity, normalized to the mean baseline intensity, in mitochondria of Miro1-K572R. ($N_{Diff} = 6$, $n_{videos/Diff} = 1$). Data are presented as mean ± SEM. Two-way ANOVA followed by Dunnett's multiple comparisons test revealed significant variation between treatments [$F(31, 372) = 150.3$; $p < 0.0001$]. Multiple comparisons: n.s.
J Quantification of the mean Rhod-2, AM intensity, normalized per mean baseline intensity, at SPLICS-short of Miro1- K572R. ($N_{Diff} = 6$, $n_{videos/Diff} = 1$). Data are presented as mean ± SEM. Two-way ANOVA followed by Dunnett's multiple comparisons test revealed significant variation between treatments [$F(31, 372) = 148.3$; $p < 0.0001$]. Multiple comparisons: n.s.
K Quantification of the SPLICS-short signal area normalized to the mitochondria area, normalized to the mean baseline SPLICS-short signal area in Miro1- K572R. ($N_{Diff} = 6$, $n_{videos/Diff} = 1$). Data are presented as mean ± SEM. Two-way ANOVA followed by Dunnett's multiple comparisons test revealed significant variation between treatments [$F(30, 360) = 39.16$; $p < 0.0001$]. Multiple comparisons: n.s.
L Quantitative analysis of the mean Rhod-2, AM intensity, normalized to the mean baseline intensity, in mitochondria of Miro1-S156A. ($N_{Diff} = 5$, $n_{videos/Diff} = 1$). Data are presented as mean ± SEM. Two-way ANOVA followed by Dunnett's multiple comparisons test revealed significant variation between treatments [$F(28, 336) = 149.6$; $p < 0.0001$]. Multiple comparisons: n.s.
M Quantification of the mean Rhod-2, AM intensity, normalized per mean baseline intensity, at SPLICS-short of Miro1- S156A. ($N_{Diff} = 5$, $n_{videos/Diff} = 1$). Data are presented as mean ± SEM. Two-way ANOVA followed by Dunnett's multiple comparisons test revealed significant effects of timepoints [$F(2.970, 86.12) = 3.602$; $p = 0.0170$] and significant variation between treatments [$F(19, 228) = 249.1$; $p < 0.0001$]. Multiple comparisons: n.s.
N Quantification of the SPLICS-short signal area normalized to the mitochondria area, normalized to the mean baseline SPLICS-short signal area in Miro1- S156A. ($N_{Diff} = 5$, $n_{videos/Diff} = 1$). Data are presented as mean ± SEM. Two-way ANOVA followed by Dunnett's multiple comparisons test revealed significant variation between treatments [$F(27, 324) = 31.83$; $p < 0.0001$]. Multiple comparisons: n.s.

Our results showed that calcium is taken up into the mitochondria at narrow MERCS primarily via the MCU. The calcium flux from the ER into the mitochondria is likely sustained by SOCE, since BTP2 abolished the thapsigargin effect. However, inhibition of the MCU phenocopies the effects of Miro1 mutations R272Q, K572R and S156A, suggesting that Miro1 regulates MCU-mediated mitochondrial calcium uptake at narrow MERCS. However, specifically the calcium flux from the ER into mitochondria at narrow MERCS (as should be induced by thapsigargin) is impaired in all Miro1 mutants, suggesting that the functionality of narrow MERCS as hub for efficient calcium flux might be compromised.

3.4. K572R and S156A mutations increase SOCE

The calcium flux from the ER into mitochondria at MERCS depends on the ER calcium level, which is maintained by SOCE (Malli et al., 2007). As we observed alterations in mitochondrial calcium homeostasis, we further aimed to investigate SOCE. First, neurons were stained with the calcium-sensitive dye Fluo-4, AM. To eliminate extracellular calcium and to prevent SOCE through CRAC channels across the plasma membrane, neurons were incubated in a calcium-free Ringer solution immediately prior to the experiment (Fig. 4A). Baseline measurements of Fluo-4, AM fluorescence intensity, indicative of cytosolic calcium levels, showed no significant alterations in Miro1-R272Q, -K572R or -S156A neurons, compared to isogenic neurons, under these conditions (Fig. 4B). Following baseline measurements, cells were treated with 10 μM thapsigargin to induce ER calcium release. All neuron lines exhibited an ER calcium release that was statistically indistinguishable to the isogenic control neurons (Fig. 4C). Subsequently, Ringer solution containing calcium was applied to trigger SOCE, and the resulting changes in cytosolic calcium levels were measured. Our results revealed a significant increase in SOCE in neurons harboring the Miro1-K572R or Miro1-S156A mutations, compared to the isogenic control. The Miro1-R272Q mutant however behaved similar to the isogenic control (Fig. 4D).

While the R272Q variant showed no abnormal properties with regard to cytosolic calcium or SOCE, changes in SOCE were particularly evident in the functional mutants K572R and S156A. This suggests that the R272Q variant, located in the calcium-binding EF1 domain, primarily disrupts mitochondrial calcium buffering capacity at narrow MERCS, whereas the functional mutants K572R and S156A additionally influence cellular calcium homeostasis via SOCE.

3.5. Miro1 mutations decrease STIM1 protein expression

Based on our findings that Miro1 mutations disrupt MERCS organization and compromise both mitochondrial calcium homeostasis and

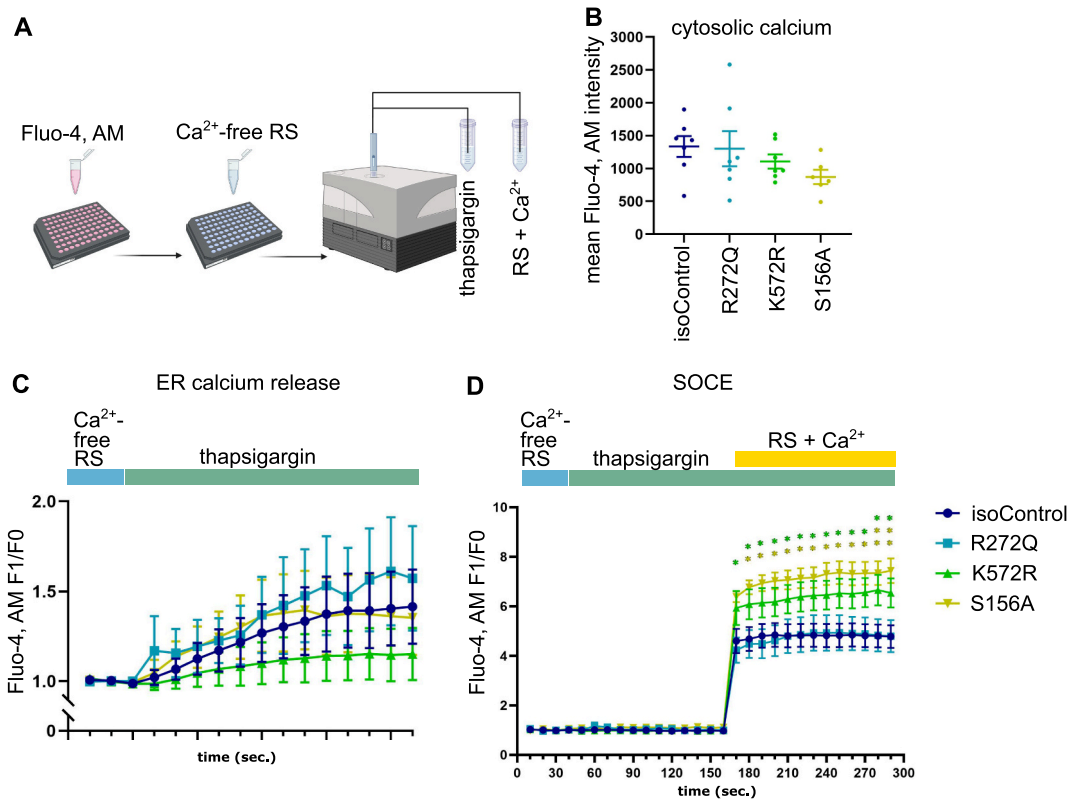

Fig. 4. Analysis of SOCE.
A Schematic representation of the experimental layout. Neurons were stained with Fluo-4, AM, incubated in calcium-free Ringer's solution (RS), and recorded in a plate reader. Thapsigargin and RS supplemented with calcium were applied during the measurements. Schematic images created with *Biorender.com*.
B Quantitative analysis of cytosolic calcium levels under baseline conditions. ($N_{Diff} = 7$). Data are presented as mean ± SEM. One-way ANOVA followed by Dunnett's multiple comparisons test revealed no significance [$F(3,23) = 1.366$; $p < 0.2779$]. Multiple comparisons: n.s.
C Calcium release from the ER was triggered by application of thapsigargin. ($N_{Diff} = 6$). Data are presented as mean ± SEM. Two-way ANOVA followed by Dunnett's multiple comparisons test revealed significant effects of timepoints [$F(1.411, 25.40) = 12.47$; $p = 0.0006$] significant variation between genotypes [$F(18, 216) = 85.18$; $p < 0.0001$]. Multiple comparisons: n.s.
D Analysis of cytosolic calcium levels after triggering SOCE with a sequential administration of calcium-free RS, thapsigargin and calcium-containing RS. ($N_{Diff} = 7$). Data are presented as mean ± SEM. Two-way ANOVA followed by Dunnett's multiple comparisons test revealed significant effects of timepoints [$F(1.510, 34.72) = 11.65$; $p = 0.0004$], significant effects of genotypes [$F(3, 23) = 6.143$; $p = 0.0032$] and significant variation between genotypes [$F(23, 276) = 270.5$; $p < 0.0001$]. Multiple comparisons: * $p \leq 0.05$, ** $p \leq 0{,}01$. RS = Ringer solution, SOCE = store operated calcium entry.

SOCE, we sought to further investigate proteins known to be involved in calcium signaling, including the voltage-dependent anion channel (VDAC) on the outer mitochondrial membrane (Sander et al., 2021), the Stromal Interaction Molecule 1 (STIM1), which is the ER calcium sensor responsible for driving SOCE (Roos et al., 2005), the MCU (Marchi and Pinton, 2014) or the MCU regulator Mitochondrial Calcium Uptake 1 (MICU1) (Perocchi et al., 2010; Mallilankaraman et al., 2012), via Western blot analysis. STIM1 was significantly reduced in all three Miro1-mutant neuronal lines compared to the isogenic control (Fig. 5A; Supplementary Fig. 1). In contrast, protein levels of VDAC (Fig. 5B; Supplementary Fig. 2), MCU (Fig. 5C; Supplementary Fig. 3) or MICU1 (Fig. 5D; Supplementary Fig. 4) were not significantly changed in any Miro1-mutant neuron line, compared to the isogenic control.

Together, these results indicate that alterations of cellular and mitochondrial calcium homeostasis in Miro1 mutant neurons are driven to some extent by alterations in SOCE, rather than alterations in mitochondrial calcium channel expression.

3.6. Inhibition of the MCU increases lipid peroxidation in Miro1 mutant neurons

Previous reports showed that impairments in calcium homeostasis were linked to lipid peroxidation, subsequently leading to ferroptosis (Campos et al., 2024; Gleitze et al., 2023). Our results demonstrated an overall misregulation of cellular calcium homeostasis in Miro1 mutant neurons. Therefore, we seeked to investigate possible downstream effects such as lipid peroxidation and cell death via ferroptosis. To this end, neurons were treated with 750 nM RSL3 to inhibit the enzyme GPX4, which is the primary enzyme responsible for replenishing of glutathione, thereby increasing ROS and inducing lipid peroxidation (Li et al., 2021). To examine the involvement of mitochondrial calcium, 750 nM RSL3 was combined with the MCU inhibitor Ru360 in order to prevent mitochondrial calcium uptake as this treatment phenocopied the impaired mitochondrial calcium buffering of the Miro1 mutants. Furthermore, 0.5 μM Liproxstatin-1 (Lip-1), a lipid peroxidation scavenger that prevents accumulation of lipid hydroperoxides (Zilka et al., 2017), was applied to rescue cells from ROS-induced lipid peroxidation (Fig. 6A).

Lipid peroxidation was assessed via Bodipy 665/676 staining (Fig. 6B). The isogenic control presented a significant increase in lipid peroxidation with RSL3, whereas Ru360 showed no additional effect on lipid peroxidation. As expected, Lip-1 counteracted the effect of RSL3 on lipid peroxidation in the isogenic control (Fig. 6C).

In Miro1-R272Q neurons RSL3 alone had no additional effect on lipid peroxidation, compared to the DMSO treatment. In contrast, RSL3 + Ru360 significantly increased lipid peroxidation, compared to R272Q neurons treated with DMSO. Lipid peroxidation was significantly reduced in Miro1-R272Q neurons treated with RSL3 + Lip-1, compared

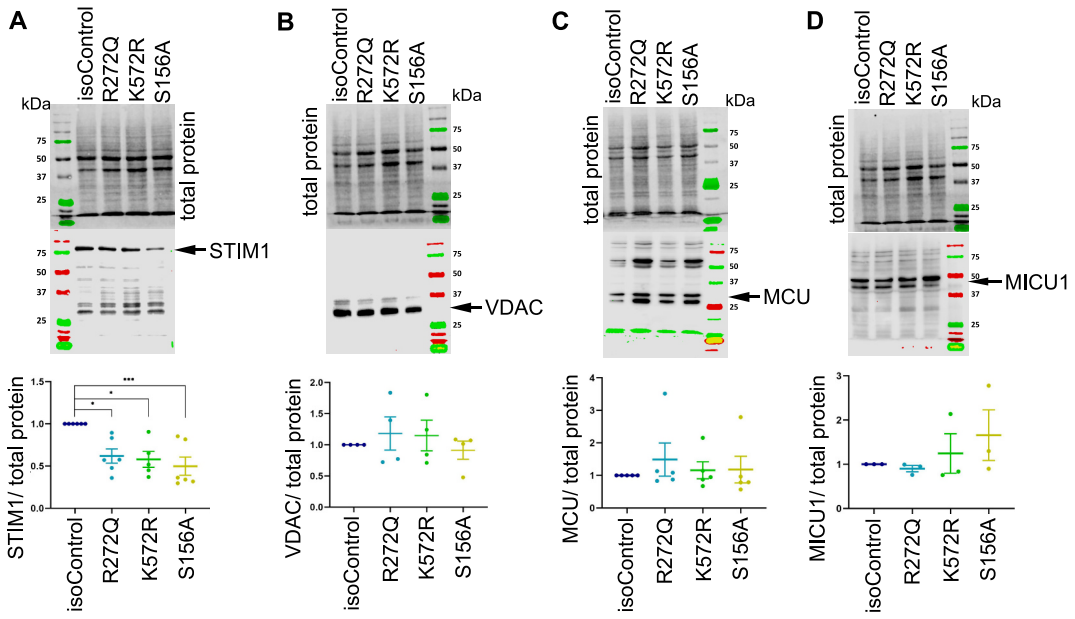

Fig. 5. Western blot analysis of proteins involved in calcium homeostasis. Analysis of protein levels of A STIM1 ($N_{Diff} = 6$), B VDAC ($N_{Diff} = 4$), C MCU ($N_{Diff} = 5$), and D MICU1 ($N_{Diff} = 3$). Values were normalized to total protein and respective protein levels of the isogenic control. Data are presented as mean ± SEM. Statistical significance was determined using the Kruskal–Wallis test. * $p \leq 0.05$, *** $p \leq 0.001$.

to RSL3 + Ru360 treatment (Fig. 6C).

Miro1-K572R neurons showed significant elevation in lipid peroxidation at baseline conditions, compared to the isogenic control. RSL3 treatment alone had no additional effect on lipid peroxidation, while RSL3 + Ru360 significantly increased lipid peroxidation, compared to DMSO. In K572R neurons treated with RSL3 + Lip-1, lipid peroxidation was comparable to isogenic control neurons treated with DMSO (Fig. 6C).

Miro1-S156A neurons showed no significantly increased lipid peroxidation under RSL3 treatment alone, while RSL3 + Ru360 significantly increased lipid peroxidation. RSL3 + Lip-1 showed significantly less lipid peroxidation compared to RSL3 + Ru360 in Miro1-S156A neurons (Fig. 6C).

Together, these data suggest that while mitochondrial calcium does not seem to play a major role in lipid peroxidation in the isogenic control, Miro1-mutant neurons were more prone to lipid peroxidation, specifically under conditions of MCU inhibition.

The next step was to analyze cell viability using AquaBluer assay. To initiate ferroptosis, neurons were again treated with RSL3 with increasing concentrations (500 nM, 750 nM, 1000 nM). Cell viability was indistinguishable between all neurons under mock conditions and Lip-1 had no effect when combined with DMSO mock treatment. RSL3 treatments led to decreased cell viability, which was restored in all lines by Lip-1, proofing that reduced viability was caused by ferroptosis. In Miro1-R272Q and Miro1-S156A neurons cell viability was significantly reduced by 500 nM RSL3 compared to the isogenic control, while Miro1-K572R neurons were indistinguishable to the isogenic control. Finally, at 750 nM and 1000 nM RSL3, all three Miro1-mutants behaved similar to the isogenic control (Fig. 6D).

The mutations with significantly altered resting mitochondrial calcium levels compared to the isogenic control - namely R272Q and S156A - also exhibit increased sensitivity to ferroptosis. Since the K572R mutant exhibits resting mitochondrial calcium levels that are consistent with the isogenic control, it may be therefore not more susceptible to ferroptosis than the isogenic control. However, the observation remains that all Miro1 mutants exhibit increased lipid peroxidation under MCU inhibition. Taken together, these results clearly indicate a link between impaired mitochondrial calcium homeostasis and lipid peroxidation, which ultimately increases the susceptibility of neurons to ferroptosis.

4. Discussion

Our study provides novel insights into Miro1 as a central regulator of ER–mitochondria communication and a comprehensive analysis of impaired intracellular calcium homeostasis in neurons with mutations in Miro1. Distinct Miro1 mutations, R272Q, K572R and S156A, produce specific disruptions in MERCS dynamics, mitochondrial calcium buffering capacity, SOCE, and susceptibility to lipid peroxidation and ferroptosis.

In our study, it is important to note that the R272Q and K572R mutations are heterozygous, while the S156A mutation is homozygous (Schwarz et al., 2021). All mutations in *RHOT1* that have been described in PD patients so far were heterozygous, including R272Q. Heterozygous fibroblasts or iPSC-derived neurons obtained from these PD patients showed significant mitochondria-related phenotypes, compared to unrelated control cells (Grossmann et al., 2019; Berenguer-Escuder et al., 2019; Berenguer-Escuder et al., 2020), or compared to a gene corrected isogenic control (Chemla et al., 2025). The heterozygous R272Q mutation introduced in a healthy background also produced significant phenotypes (Schwarz et al., 2022). Additionally, mice with the heterozygous R285Q mutation, the mouse orthologue to human R272Q, showed significant decline of dopaminergic neurons (Chemla et al., 2025). Knockdown of *RHOT1* in M17 cells and overexpression of Miro1-R272Q indicated that this Miro1 mutation caused a gain of function (Grossmann et al., 2019). Nevertheless, when interpreting our results, one should take into account the heterozygosity or homozygosity of the various mutations and the resulting potential dosage effects.

While Miro1's role in calcium homeostasis has been recognized in numerous publications (Fransson et al., 2006; MacAskill et al., 2009; Niescier et al., 2018; Saotome et al., 2008), its specific impact on MERCS is an emerging topic. MERCS fine-tune calcium signaling and metabolic communication between ER and mitochondria (Lim et al., 2021; Cieri et al., 2018; Giacomello and Pellegrini, 2016). Disruption of these contacts has been linked to neurodegeneration in PD (Larrañaga-SanMiguel et al., 2025; Valadas et al., 2018). We demonstrate that Miro1-K572R and -S156A, but not the -R272Q, mutations showed increased narrow MERCS abundance. Berenguer-Escuder and colleagues previously reported that the Miro1-R272Q variant increased the overall

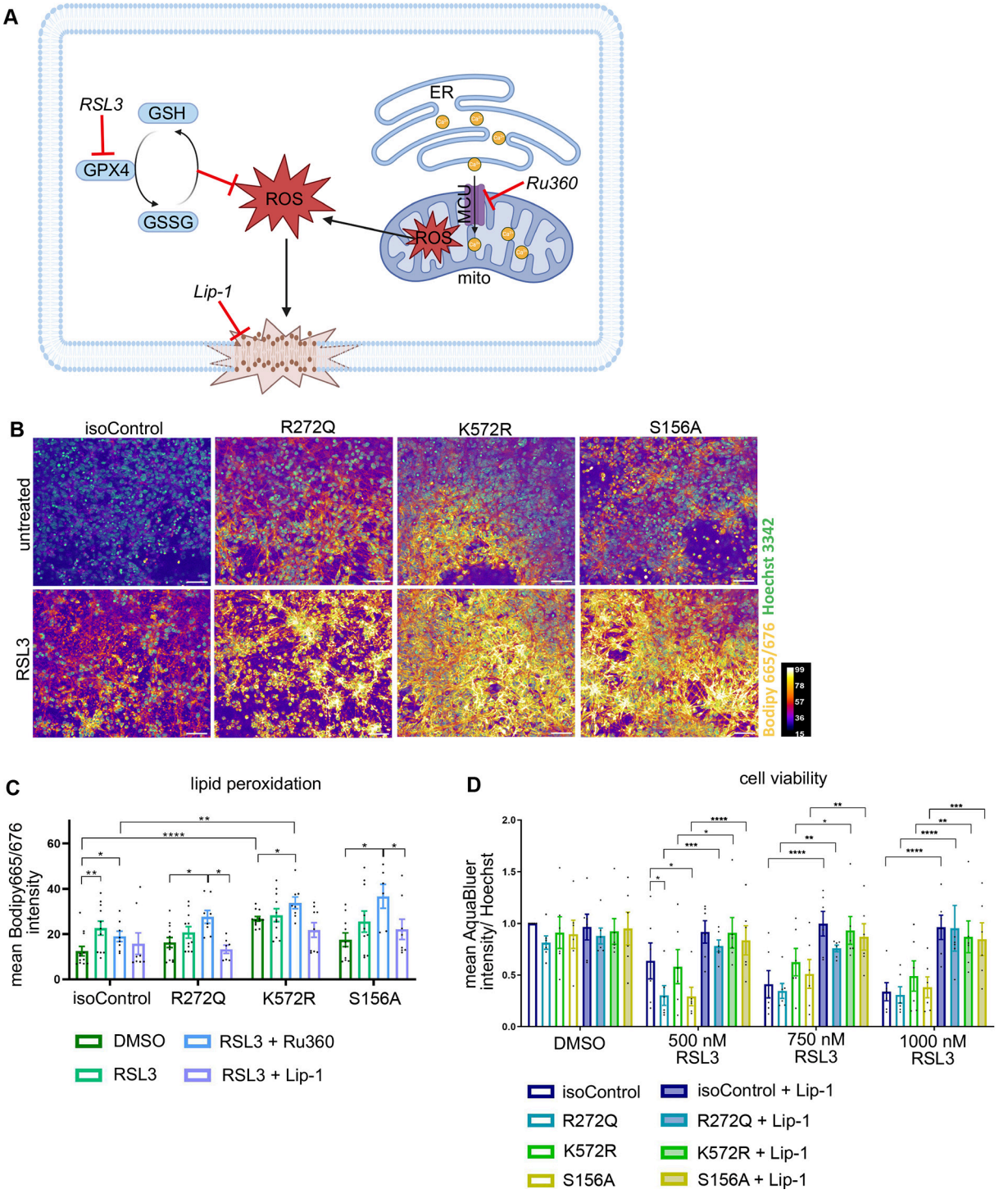

Fig. 6. Quantitative analysis of lipid peroxidation and cell viability.

A Schematic illustration of the ferroptosis pathway and pharmacological treatments applied. Neurons were treated with RSL3 to induce ferroptotic cell death or with Liproxstatin-1 (Lip-1) to inhibit lipid peroxidation. The mitochondrial calcium uniporter (MCU) was inhibited by 10 μM Ru360. Schematic images created with *Biorender.com*.

B Lipid peroxidation was assessed by using the lipid peroxidation-sensitive BODIPY 665/676 (LUT fire). Nuclei were counterstained by Hoechst 33342 (green). Scale bar indicates 50 μm. Images were obtained with a LSM900 Axio Observer Z1/7 microscope using a Plan-Apochromat 20×/0.8 M27 objective (Zeiss).

C Quantification of lipid peroxidation by mean BODIPY 665/676 intensity, normalized to nuclei. ($N_{Diff} = 6$; $n_{Images/Diff} = 2$). Data are presented as mean ± SEM. Mixed-effects model followed by Tukey's multiple comparisons test revealed significant effects of genotypes [$F(3, 42) = 4.630$; $p = 0.0069$] and significant effects of treatments [$F(2.329, 72.19) = 17.69$; $p < 0.0001$]. Multiple comparisons: $^{*}p \leq 0.05$, $^{**}p \leq 0.01$, $^{****}p \leq 0.0001$.

D Cell viability was assessed by quantification of AquaBluer fluorescence intensity, normalized to Hoechst. ($N_{Diff} = 6$). Data are presented as mean ± SEM. Two-way ANOVA followed by Tukey's multiple comparisons test revealed significant effects of treatments [$F(3, 15) = 17.14$; $p < 0.0001$], significant effects of genotypes [$F(7, 35) = 4.448$; $p = 0.0013$] and significant interactions between genotypes and treatments [$F(21, 105) = 4.092$; $p < 0.0001$]. Multiple comparison: $^{*}p \leq 0.05$, $^{**}p \leq 0,01$, $^{***}p \leq 0.001$, $^{****}p \leq 0.0001$. (For interpretation of the references to colour in this figure legend, the reader is referred to the web version of this article.)

abundance in MERCS in neurons (Berenguer-Escuder et al., 2020). In contrast to our isogenic model (Schwarz et al., 2021; Schwarz et al., 2022), the study of Berenguer-Escuder and colleagues used iPSC-derived neurons from a PD patient and an independent control donor. Additionally, MERCS abundance was assessed by the colocalization of the ER protein Calnexin and the mitochondrial protein Tom20 from immunstainings (Berenguer-Escuder et al., 2020). Hence, differences in results between the studies may occur due to differences in applied cell models and methodology. However, the dynamic reorganization of narrow MERCS under thapsigargin-induced calcium stress was affected in all three Miro1 mutants, highlighting the importance for Miro1 in the dynamic regulation of MERCS.

An increase in wide MERCS, i.e. SPLICS-long, was only observed in S156A mutant neurons. Wide MERCS were associated with mitophagy as they i) provide a hub for lipid transfer necessary for the formation of autophagosomes (Cieri et al., 2018; Hamasaki et al., 2013; van Vliet et al., 2024) and ii) need to be dissociated in order to liberate damaged mitochondria from the ER for subsequent mitophagy. A pre-requisite for this process is the PINK1/Parkin-mediated degradation of MERCS-associated proteins, such as Miro1 or mitofusin 2. Impaired Miro1 degradation in damaged mitochondria is closely linked to defective initiation of mitophagy in genetic and sporadic PD models (Hsieh et al., 2019; Drwesh et al., 2025; Hsieh et al., 2016). Intriguingly, in iPSC-derived neurons from a PD patient with mutations in Parkin, mitofusin 2 was resistant to degradation upon CCCP-induced mitochondrial damage, thereby stabilizing wide MERCS and hindering mitophagy (McLelland et al., 2018). In this context, it is particularly interesting that in Miro1-S156A neurons—but not in Miro1-R272Q neurons— Miro1 and mitofusin 2 were resistant to degradation following CCCP-induced mitochondrial damage (Schwarz and Fitzgerald, 2022; Schwarz et al., 2022). We therefore propose that Miro1-S156A is resistant to mitochondrial-damage induced degradation and may consequently possess more stable and more abundant wide MERCS. It remains unclear whether the absence of this finding in R272Q (and, at least as far as wide MERCS are concerned, also in K572R) is caused by the cells being heterozygous.

Previous studies focused on the analysis of cytosolic calcium in Miro1 mutant cells, using the cytosolic calcium dye Fluo-4, AM. Fibroblasts with the heterozygous mutation R272Q, or non-isogenic iPSC-derived Miro1-R272Q neurons obtained from PD patients displayed prolonged cytosolic calcium elevation after thapsigargin administration, indirectly suggesting impaired cellular calcium buffering capacity (Grossmann et al., 2019; Berenguer-Escuder et al., 2019; Berenguer-Escuder et al., 2020). Schwarz and colleagues showed that the decline of thapsigargin-induced cytosolic calcium peaks was similar in isogenic Miro1-R272Q iPSC-derived neurons and the isogenic control (Schwarz et al., 2022). However, to our knowledge, the mitochondrial calcium uptake capacity has not previously been directly investigated in Miro1 mutant neurons.

Of note, all three mutants, R272Q, K572R and S156A, displayed a diminished mitochondrial calcium uptake capacity upon thapsigargin-induced calcium stress. As baseline mitochondrial calcium levels were not reduced in any mutant, it can be concluded that mitochondria in Miro1 mutant neurons are in general able to take up calcium, but the spare calcium buffering capacity under stress seems to be affected. Miro1 localizes at MERCS, regulating cytosolic and mitochondrial calcium (Lee et al., 2016) by direct interaction with MCU and VDAC (Ren et al., 2023; Kamer et al., 2017; Niescier et al., 2018). The expression of these calcium channels was not affected in Miro1 mutant neurons, implying that there was no general disruption of MCU or VDAC contributing in the observed calcium phenotypes. However, MCU inhibition via Ru360 phenocopied the impaired thapsigargin-induced mitochondrial calcium buffering of Miro1 mutants in the isogenic control. MCU inhibition by Mitoxantrone likewise phenocopied the alterations observed in cytosolic calcium handling in Miro1-R272Q neurons (Schwarz et al., 2022), implying a misregulation of MCU-mediated mitochondrial calcium uptake at MERCS in Miro1 mutant neurons. Local distribution of basal calcium levels in the mitochondria compartment varied greatly among the different Miro1 mutants. While the R272Q mutant was characterized primarily by the absence of a calcium gradient between MERCS and the mitochondrial compartment, calcium levels in the K572R mutant were comparable to those in the isogenic control, whereas those in the S156A mutant were significantly elevated. We therefore conclude that calcium flux at MERCS is a common issue in all Miro1 mutants, which is further influenced by mutation-specific factors.

One possible factor may stem from the question of why the functional mutants K572R and S156A—which cannot be ubiquitinated by Parkin or phosphorylated by PINK1, respectively— have any effect on calcium homeostasis at all. The PD-associated mutant R272Q is located in the calcium-binding EF-hand domain (Grossmann et al., 2019), which is why calcium-related phenotypes don't come as surprise. Parkin plays a direct role in calcium homeostasis by regulating various proteins, e.g. VDAC (Ham et al., 2020), Miro1 (Wang et al., 2011; Birsa et al., 2014; Hsieh et al., 2016), or MICU1 (Matteucci et al., 2018). PINK1s role in calcium homeostasis is less well understood. However, loss of PINK1 causes alterations in mitochondrial calcium levels (Grossmann et al., 2023; Gandhi et al., 2009) and PINK1 phosphorylates the mitochondrial calcium transporter leucine zipper-EF-hand-containing transmembrane protein 1 (LETM1) (Huang et al., 2017). Both, PINK1 and Parkin, influence calcium homeostasis by regulating MERCS (Calì et al., 2013; Grossmann et al., 2023; Basso et al., 2018). We were able to show that iPSC-derived neurons with PD-associated mutations in PINK1 or Parkin also exhibited impaired dynamic adaptation of narrow MERCS under thapsigargin stress similar to the Miro1 mutants, albeit with subtle differences in their otherwise calcium phenotypes (Grossmann et al., 2023). This leads us to conclude that the lack of regulation of Miro1-S156A or K572R and the respective MERCS by PINK1 or Parkin, respectively, may be a factor in the development of the corresponding calcium phenotypes.

Fitting to the study of Schwarz and colleagues (Schwarz et al., 2022), we did not observe alterations in thapsigargin-induced ER calcium release in any of the Miro1 mutants. S156A and K572R neurons showed enhanced SOCE, which is triggered by STIM1 translocation, and CRAC channel activation upon ER calcium store depletion (Stathopulos et al., 2013). Notably, the CRAC inhibitor BTP2 partially rescued calcium phenotypes in Miro1-R272Q and S156A mutant neurons. These observations suggest that SOCE plays a pivotal role in the calcium dyshomeostasis caused by Miro1 mutations.

Finally, inhibition of the MCU with Ru360 increased lipid peroxidation in all three neurons with Miro1 mutation, and R272Q and S156A neurons were more susceptible to ferroptosis compared to the isogenic control. The literature shows that MCU inhibition can have opposing effects on lipid peroxidation and ferroptosis. While some studies found an alleviating effect of MCU inhibition by Ru265, Mitoxantrone or MCU-i4 on ferroptosis in HT22 cells or by MCU knockout in mice (Marmolejo-Garza et al., 2023; Fefelova et al., 2023), other groups reported that MCU-i4 in BT474 cells or expression of a dominant negative MCU mutant in cardiomyocytes caused an increase in cytoplasmic calcium levels, leading to major metabolic changes and ROS production, resulting in increased sensitivity to cell death (Rasmussen et al., 2015; So et al., 2025). Fitting, iPSC-derived neurons from a PD patient with the heterozygous R272Q mutation exhibited elevated ROS levels and increased cell death compared to the gene corrected isogenic control (Chemla et al., 2025). Furthermore, cell death was significantly increased in isogenic R272Q neurons by staurosporine (Schwarz et al., 2022), which causes apoptosis by elevating cytosolic calcium levels and ROS production (Rabkin and Kong, 2002; Kruman et al., 1998; Jones and Sharpe, 1994; Seo and Seo, 2009). In this context, it should be emphasized that ferroptosis was induced particularly in the Miro1 mutants R272Q and S156A, which also exhibited changes in calcium distribution at mitochondria and narrow MERCS or increased

mitochondrial calcium levels, respectively, whereas K572R behaved comparable to the isogenic control in terms of basal mitochondrial calcium levels and the induction of ferroptosis. Together, these findings suggest lipid peroxidation as a downstream consequence of disrupted calcium homeostasis caused by mutations in Miro1, leading to increased vulnerability to ferroptosis particularly in R272Q and S156A neurons.

In summary, distinct Miro1 mutations converge on impaired mitochondrial calcium homeostasis and impaired calcium-regulated MERCS dynamics, specifically under conditions of elevated calcium stress. Additionally, our study points to major dysregulation of cellular calcium homeostasis that exceeds the involvement of mitochondria and MERCS, including alterations in SOCE. We propose that this calcium dysregulation renders Miro1 mutant neurons more vulnerable to lipid peroxidation and ferroptosis. These insights provide a mechanistic framework for how Miro1 dysfunction contributes to neuronal demise in PD and suggest that restoring calcium balance through MERCS or SOCE modulation could be a promising therapeutic strategy in the future.

Supplementary data to this article can be found online at https://doi.org/10.1016/j.nbd.2026.107492.

CRediT authorship contribution statement

Anna E. Bartalis: Writing – original draft, Visualization, Methodology, Investigation, Formal analysis, Data curation. **Jack Genschmar:** Investigation, Formal analysis, Data curation. **Julia C. Fitzgerald:** Writing – review & editing, Resources, Methodology. **Andreas Hermann:** Writing – review & editing, Supervision, Project administration, Funding acquisition, Resources, Conceptualization. **Dajana Grossmann:** Writing – review & editing, Writing – original draft, Visualization, Supervision, Project administration, Methodology, Investigation, Funding acquisition, Formal analysis, Data curation, Conceptualization.

Funding

This work was supported, in part, by the German Society for Parkinson's disease and movement disorders (DPG) to DG. AH is supported by the Hermann and Lilly Schilling-Stiftung für medizinische Forschung im Stifterverband. The LSM900 AxioObserver.Z1 Airyscan 2 microscope (Zeiss) was funded by the German Research Foundation (DFG: INST 264/175-1 FUGG). DG received funds from the German Research Foundation (DFG: GR 6326/2-1). JF received funds from the German Research Foundation (DFG: RTG 2364 “MOMbrane”).

Declaration of competing interest

AH has received funding from the European Social Fonds, the Federal Ministry of Education and Research and the Hermann and Lilly Schilling-Stiftung für medizinische Forschung im Stifterverband. He has received honoraria for presentations and participation in advisory boards from Amylyx and IFT Pharma. He has received royalties from Elsevier Press and Kohlhammer.

Data availability

Data are available from the corresponding author upon reasonable request.

References

Barazzuol, Lucia, Giamogante, Flavia, Brini, Marisa, Calì, Tito, 2020. PINK1/Parkin mediated mitophagy, Ca2+ signalling, and ER-mitochondria contacts in Parkinson’s disease. Int. J. Mol. Sci. 21 (5). https://doi.org/10.3390/ijms21051772.

Basso, Valentina, Marchesan, Elena, Peggion, Caterina, Chakraborty, Joy, von Stockum, Sophia, Giacomello, Marta, et al., 2018. Regulation of ER-mitochondria contacts by Parkin via Mfn2. Pharmacol. Res. 138, 43–56. https://doi.org/10.1016/j.phrs.2018.09.006.

Berenguer-Escuder, Clara, Grossmann, Dajana, Massart, François, Antony, Paul, Burbulla, Lena F., Glaab, Enrico, et al., 2019. Variants in Miro1 cause alterations of ER-mitochondria contact sites in fibroblasts from Parkinson’s disease patients. J. Clin. Med. 8 (12). https://doi.org/10.3390/jcm8122226.

Berenguer-Escuder, Clara, Grossmann, Dajana, Antony, Paul, Arena, Giuseppe, Wasner, Kobi, Massart, François, et al., 2020. Impaired mitochondrial-endoplasmic reticulum interaction and mitophagy in Miro1-mutant neurons in Parkinson’s disease. Hum. Mol. Genet. 29 (8), 1353–1364. https://doi.org/10.1093/hmg/ddaa066.

Birsa, Nicol, Norkett, Rosalind, Wauer, Tobias, Mevissen, Tycho E.T., Wu, Hsiu-Chuan, Foltynie, Thomas, et al., 2014. Lysine 27 ubiquitination of the mitochondrial transport protein Miro is dependent on serine 65 of the Parkin ubiquitin ligase. J. Biol. Chem. 289 (21), 14569–14582. https://doi.org/10.1074/jbc.M114.563031.

Calì, Tito, Ottolini, Denis, Negro, Alessandro, Brini, Marisa, 2013. Enhanced parkin levels favor ER-mitochondria crosstalk and guarantee Ca(2+) transfer to sustain cell bioenergetics. Biochim. Biophys. Acta 1832 (4), 495–508. https://doi.org/10.1016/j.bbadis.2013.01.004.

Campos, Joaquín, Gleitze, Silvia, Hidalgo, Cecilia, Núñez, Marco T., 2024. IP3R-mediated calcium release promotes ferroptotic death in SH-SY5Y neuroblastoma cells. Antioxidants (Basel, Switzerland) 13 (2). https://doi.org/10.3390/antiox13020196.

Chan, C. Savio, Gertler, Tracy S., Surmeier, D. James, 2009. Calcium homeostasis, selective vulnerability and Parkinson’s disease. Trends Neurosci. 32 (5), 249–256. https://doi.org/10.1016/j.tins.2009.01.006.

Chang, Karen T., Niescier, Robert F., Min, Kyung-Tai, 2011. Mitochondrial matrix Ca2+ as an intrinsic signal regulating mitochondrial motility in axons. Proc. Natl. Acad. Sci. USA 108 (37), 15456–15461. https://doi.org/10.1073/pnas.1106862108.

Chemla, Axel, Arena, Giuseppe, Sacripanti, Ginevra, Barmpa, Kyriaki, Zagare, Alise, Garcia, Pierre, et al., 2025. Parkinson's disease mutant Miro1 causes mitochondrial dysfunction and dopaminergic neuron loss. Brain J. Neurol. 148 (10), 3607–3622. https://doi.org/10.1093/brain/awaf051.

Cieri, Domenico, Vicario, Mattia, Giacomello, Marta, Vallese, Francesca, Filadi, Riccardo, Wagner, Tina, et al., 2018. SPLICS: a split green fluorescent protein-based contact site sensor for narrow and wide heterotypic organelle juxtaposition. Cell Death Differ. 25 (6), 1131–1145. https://doi.org/10.1038/s41418-017-0033-z.

Drwesh, Layla, Arena, Giuseppe, Merk, Daniel J., Ferrante, Daniele, Gorgogietas, Vyron, Gasser, Thomas, et al., 2025. Methodological validation of Miro1 retention as a candidate Parkinson's disease biomarker. NPJ Parkinsons Dis. 11 (1), 270. https://doi.org/10.1038/s41531-025-01115-8.

Endoni, Benney T., Koval, Olha M., Allamargot, Chantal, Kortlever, Tara, Qian, Lan, Sadoski, Riley J., et al., 2025. MIRO1 is required for dynamic increases in mitochondria-ER contact sites and mitochondrial ATP during the cell cycle. Cells 14 (7). https://doi.org/10.3390/cells14070482.

Fefelova, Nadezhda, Wongjaikam, Suwakon, Pamarthi, Sri Harika, Siri-Angkul, Natthaphat, Comollo, Thomas, Kumari, Anshu, et al., 2023. Deficiency of mitochondrial calcium uniporter abrogates iron overload-induced cardiac dysfunction by reducing ferroptosis. Basic Res. Cardiol. 118 (1), 21. https://doi.org/10.1007/s00395-023-00990-7.

Forno, L.S., 1996. Neuropathology of Parkinson’s disease. J. Neuropathol. Exp. Neurol. 55 (3), 259–272. https://doi.org/10.1097/00005072-199603000-00001.

Fransson, Sa, Ruusala, Aino, Aspenström, Pontus, 2006. The atypical rho GTPases Miro-1 and Miro-2 have essential roles in mitochondrial trafficking. Biochem. Biophys. Res. Commun. 344 (2), 500–510. https://doi.org/10.1016/j.bbrc.2006.03.163.

Gandhi, Sonia, Wood-Kaczmar, Alison, Yao, Zhi, Plun-Favreau, Helene, Deas, Emma, Klupsch, Kristina, et al., 2009. PINK1-associated Parkinson’s disease is caused by neuronal vulnerability to calcium-induced cell death. Mol. Cell 33 (5), 627–638. https://doi.org/10.1016/j.molcel.2009.02.013.

Giacomello, M., Pellegrini, L., 2016. The coming of age of the mitochondria-ER contact: a matter of thickness. Cell Death Differ. 23 (9), 1417–1427. https://doi.org/10.1038/cdd.2016.52.

Gleitze, Silvia, Ramírez, Omar A., Vega-Vásquez, Ignacio, Yan, Jing, Lobos, Pedro, Bading, Hilmar, et al., 2023. Ryanodine receptor mediated calcium release contributes to ferroptosis induced in primary hippocampal neurons by GPX4 inhibition. Antioxidants (Basel, Switzerland) 12 (3). https://doi.org/10.3390/antiox12030705.

Grossmann, Dajana, Berenguer-Escuder, Clara, Bellet, Marie Estelle, Scheibner, David, Bohler, Jill, Massart, Francois, et al., 2019. Mutations in RHOT1 disrupt endoplasmic reticulum-mitochondria contact sites interfering with calcium homeostasis and mitochondrial dynamics in Parkinson’s disease. Antioxid. Redox Signal. 31 (16), 1213–1234. https://doi.org/10.1089/ars.2018.7718.

Grossmann, Dajana, Malburg, Nina, Glaß, Hannes, Weeren, Veronika, Sondermann, Verena, Pfeiffer, Julia F., et al., 2023. Mitochondria-endoplasmic reticulum contact sites dynamics and calcium homeostasis are differentially disrupted in PINK1-PD or PRKN-PD neurons. Mov. Disord. 38 (10), 1822–1836. https://doi.org/10.1002/mds.29525.

Grossmann, Dajana, Spranger, Adrian, Fischer, Emily, Schubarth, Johanna W., Leopold, Jenny, Glaß, Hannes, et al., 2026. VPS13A deficiency leads to impaired lipid distribution and alteration of mitochondrial calcium homeostasis in fibroblasts of VPS13A disease patients. Mov. Disord. https://doi.org/10.1002/mds.70177.

Guillén-Samander, Andrés, Leonzino, Marianna, Hanna, Michael G., Tang, Ni, Shen, Hongying, de Camilli, Pietro, 2021. VPS13D bridges the ER to mitochondria and peroxisomes via Miro. J. Cell Biol. 220 (5). https://doi.org/10.1083/jcb.202010004.

Guiney, Stephanie J., Adlard, Paul A., Bush, Ashley I., Finkelstein, David I., Ayton, Scott, 2017. Ferroptosis and cell death mechanisms in Parkinson’s disease. Neurochem. Int. 104, 34–48. https://doi.org/10.1016/j.neuint.2017.01.004.

Ham, Su Jin, Lee, Daewon, Yoo, Heesuk, Jun, Kyoungho, Shin, Heejin, Chung, Jongkyeong, 2020. Decision between mitophagy and apoptosis by Parkin via

VDAC1 ubiquitination. Proc. Natl. Acad. Sci. USA 117 (8), 4281–4291. https://doi.org/10.1073/pnas.1909814117.
Hamasaki, Maho, Furuta, Nobumichi, Matsuda, Atsushi, Nezu, Akiko, Yamamoto, Akitsugu, Fujita, Naonobu, et al., 2013. Autophagosomes form at ER-mitochondria contact sites. Nature 495 (7441), 389–393. https://doi.org/10.1038/nature11910.
Hsieh, Chung-Han, Shaltouki, Atossa, Gonzalez, Ashley E., Da Bettencourt Cruz, Alexandre, Burbulla, Lena F., St Lawrence, Erica, et al., 2016. Functional impairment in Miro degradation and mitophagy is a shared feature in familial and sporadic Parkinson's disease. Cell Stem Cell 19 (6), 709–724. https://doi.org/10.1016/j.stem.2016.08.002.
Hsieh, Chung-Han, Li, Li, Vanhauwaert, Roeland, Nguyen, Kong T., Davis, Mary D., Bu, Guojun, et al., 2019. Miro1 marks Parkinson's disease subset and Miro1 reducer rescues neuron loss in Parkinson's models. Cell Metab. 30 (6), 1131–1140 e7. https://doi.org/10.1016/j.cmet.2019.08.023.
Huang, En, Qu, Dianbo, Huang, Tianwen, Rizzi, Nicoletta, Boonying, Wassamon, Krolak, Dorothy, et al., 2017. PINK1-mediated phosphorylation of LETM1 regulates mitochondrial calcium transport and protects neurons against mitochondrial stress. Nat. Commun. 8 (1), 1399. https://doi.org/10.1038/s41467-017-01435-1.
Jones, K.T., Sharpe, G.R., 1994. Staurosporine, a non-specific PKC inhibitor, induces keratinocyte differentiation and raises intracellular calcium, but Ro31-8220, a specific inhibitor, does not. J. Cell. Physiol. 159 (2), 324–330. https://doi.org/10.1002/jcp.1041590215.
Kamer, Kimberli J., Grabarek, Zenon, Mootha, Vamsi K., 2017. High-affinity cooperative Ca2+ binding by MICU1-MICU2 serves as an on-off switch for the uniporter. EMBO Rep. 18 (8), 1397–1411. https://doi.org/10.15252/embr.201643748.
Klein, Christine, Westenberger, Ana, 2012. Genetics of Parkinson's disease. Cold Spring Harb. Perspect. Med. 2 (1), a008888. https://doi.org/10.1101/cshperspect.a008888.
Klosowiak, Julian L., Focia, Pamela J., Chakravarthy, Srinivas, Landahl, Eric C., Freymann, Douglas M., Rice, Sarah E., 2013. Structural coupling of the EF hand and C-terminal GTPase domains in the mitochondrial protein Miro. EMBO Rep. 14 (11), 968–974. https://doi.org/10.1038/embor.2013.151.
Klosowiak, Julian L., Park, Sungjin, Smith, Kyle P., French, Michael E., Focia, Pamela J., Freymann, Douglas M., Rice, Sarah E., 2016. Structural insights into Parkin substrate lysine targeting from minimal Miro substrates. Sci. Rep. 6, 33019. https://doi.org/10.1038/srep33019.
Kornmann, Benoît, Osman, Christof, Walter, Peter, 2011. The conserved GTPase Gem1 regulates endoplasmic reticulum-mitochondria connections. Proc. Natl. Acad. Sci. USA 108 (34), 14151–14156. https://doi.org/10.1073/pnas.1111314108.
Kruman, I., Guo, Q., Mattson, M.P., 1998. Calcium and reactive oxygen species mediate staurosporine-induced mitochondrial dysfunction and apoptosis in PC12 cells. J. Neurosci. Res. 51 (3), 293–308. https://doi.org/10.1002/(SICI)1097-4547(19980201)51:3<293::AID-JNR3>3.0.CO;2-B.
Larrañaga-SanMiguel, Alvaro, Bengoa-Vergniory, Nora, Flores-Romero, Hector, 2025. Crosstalk between mitochondria-ER contact sites and the apoptotic machinery as a novel health meter. Trends Cell Biol. 35 (1), 33–45. https://doi.org/10.1016/j.tcb.2024.08.007.
Lee, Seongsoo, Lee, Kyu-Sun, Huh, Sungun, Liu, Song, Lee, Do-Yeon, Hong, Seung Hyun, et al., 2016. Polo kinase phosphorylates Miro to control ER-mitochondria contact sites and mitochondrial Ca(2+) homeostasis in neural stem cell development. Dev. Cell 37 (2), 174–189. https://doi.org/10.1016/j.devcel.2016.03.023.
Li, Shengbiao, He, Yuping, Chen, Kexin, Sun, Jiaojiao, Zhang, Lulu, He, Yaxin, et al., 2021. RSL3 drives ferroptosis through NF-κB pathway activation and GPX4 depletion in glioblastoma. Oxidative Med. Cell. Longev. 2021, 2915019. https://doi.org/10.1155/2021/2915019.
Lim, Dmitry, Dematteis, Giulia, Tapella, Laura, Genazzani, Armando A., Calì, Tito, Brini, Marisa, Verkhratsky, Alexei, 2021. Ca2+ handling at the mitochondria-ER contact sites in neurodegeneration. Cell Calcium 98, 102453. https://doi.org/10.1016/j.ceca.2021.102453.
Liu, C., Hermann, T.E., 1978. Characterization of ionomycin as a calcium ionophore. J. Biol. Chem. 253 (17), 5892–5894.
Ludtmann, Marthe H.R., Abramov, Andrey Y., 2018. Mitochondrial calcium imbalance in Parkinson's disease. Neurosci. Lett. 663, 86–90. https://doi.org/10.1016/j.neulet.2017.08.044.
Lytton, J., Westlin, M., Hanley, M.R., 1991. Thapsigargin inhibits the sarcoplasmic or endoplasmic reticulum Ca-ATPase family of calcium pumps. J. Biol. Chem. 266 (26), 17067–17071.
MacAskill, Andrew F., Brickley, Kieran, Stephenson, F. Anne, Kittler, Josef T., 2009. GTPase dependent recruitment of Grif-1 by Miro1 regulates mitochondrial trafficking in hippocampal neurons. Mol. Cell. Neurosci. 40 (3), 301–312. https://doi.org/10.1016/j.mcn.2008.10.016.
Mahoney-Sánchez, Laura, Bouchaoui, Hind, Ayton, Scott, Devos, David, Duce, James A., Devedjian, Jean-Christophe, 2021. Ferroptosis and its potential role in the physiopathology of Parkinson's disease. Prog. Neurobiol. 196, 101890. https://doi.org/10.1016/j.pneurobio.2020.101890.
Malli, R., Frieden, M., Hunkova, M., Trenker, M., Graier, W.F., 2007. Ca2+ refilling of the endoplasmic reticulum is largely preserved albeit reduced Ca2+ entry in endothelial cells. Cell Calcium 41 (1), 63–76. https://doi.org/10.1016/j.ceca.2006.05.001.
Mallilankaraman, Karthik, Doonan, Patrick, Cárdenas, César, Chandramoorthy, Harish C., Müller, Marioly, Miller, Russell, et al., 2012. MICU1 is an essential gatekeeper for MCU-mediated mitochondrial Ca(2+) uptake that regulates cell survival. Cell 151 (3), 630–644. https://doi.org/10.1016/j.cell.2012.10.011.
Marchi, Saverio, Pinton, Paolo, 2014. The mitochondrial calcium uniporter complex: molecular components, structure and physiopathological implications. J. Physiol. 592 (5), 829–839. https://doi.org/10.1113/jphysiol.2013.268235.
Marmolejo-Garza, Alejandro, Krabbendam, Inge E., Luu, Minh Danh Anh, Brouwer, Famke, Trombetta-Lima, Marina, Unal, Osman, et al., 2023. Negative modulation of mitochondrial calcium uniporter complex protects neurons against ferroptosis. Cell Death Dis. 14 (11), 772. https://doi.org/10.1038/s41419-023-06290-1.
Matteucci, Alessandra, Patron, Maria, Vecellio Reane, Denis, Gastaldello, Stefano, Amoroso, Salvatore, Rizzuto, Rosario, et al., 2018. Parkin-dependent regulation of the MCU complex component MICU1. Sci. Rep. 8 (1), 14199. https://doi.org/10.1038/s41598-018-32551-7.
McLelland, Gian-Luca, Goiran, Thomas, Yi, Wei, Dorval, Geneviève, Chen, Carol X., Lauinger, Nadine D., et al., 2018. Mfn2 ubiquitination by PINK1/parkin gates the p97-dependent release of ER from mitochondria to drive mitophagy. eLife 7. https://doi.org/10.7554/eLife.32866.
Modi, Souvik, López-Doménech, Guillermo, Halff, Elise F., Covill-Cooke, Christian, Ivankovic, Davor, Melandri, Daniela, et al., 2019. Miro clusters regulate ER-mitochondria contact sites and link cristae organization to the mitochondrial transport machinery. Nat. Commun. 10 (1), 4399. https://doi.org/10.1038/s41467-019-12382-4.
Niescier, Robert F., Hong, Kido, Park, Dongkeun, Min, Kyung-Tai, 2018. MCU interacts with Miro1 to modulate mitochondrial functions in neurons. J. Neurosci. 38 (20), 4666–4677. https://doi.org/10.1523/JNEUROSCI.0504-18.2018.
Patergnani, Simone, Suski, Jan M., Agnoletto, Chiara, Bononi, Angela, Bonora, Massimo, de Marchi, Elena, et al., 2011. Calcium signaling around mitochondria associated membranes (MAMs). Cell Commun. Signal 9, 19. https://doi.org/10.1186/1478-811X-9-19.
Perocchi, Fabiana, Gohil, Vishal M., Girgis, Hany S., Bao, X. Robert, McCombs, Janet E., Palmer, Amy E., Mootha, Vamsi K., 2010. MICU1 encodes a mitochondrial EF hand protein required for Ca(2+) uptake. Nature 467 (7313), 291–296. https://doi.org/10.1038/nature09358.
Pozo Devoto, Victorio M., Falzone, Tomas L., 2017. Mitochondrial dynamics in Parkinson's disease: a role for α-synuclein? Dis. Model. Mech. 10 (9), 1075–1087. https://doi.org/10.1242/dmm.026294.
Qin, Jinshan, Guo, Yuting, Xue, Boxin, Shi, Peng, Chen, Yang, Su, Qian Peter, et al., 2020. ER-mitochondria contacts promote mtDNA nucleoids active transportation via mitochondrial dynamic tubulation. Nat. Commun. 11 (1), 4471. https://doi.org/10.1038/s41467-020-18202-4.
Rabkin, Simon W., Kong, Jennifer Y., 2002. Discordance between the effect of modulators of calcium on staurosporine-induced apoptosis and staurosporine-induced actin degradation. Cell Biol. Int. 26 (5), 433–440. https://doi.org/10.1006/cbir.2002.0876.
Rasmussen, Tyler P., Wu, Yuejin, Joiner, Mei-ling A., Koval, Olha M., Wilson, Nicholas R., Luczak, Elizabeth D., et al., 2015. Inhibition of MCU forces extramitochondrial adaptations governing physiological and pathological stress responses in heart. Proc. Natl. Acad. Sci. USA 112 (29), 9129–9134. https://doi.org/10.1073/pnas.1504705112.
Reinhardt, Peter, Glatza, Michael, Hemmer, Kathrin, Tsytsyura, Yaroslav, Thiel, Cora S., Höing, Susanne, et al., 2013. Derivation and expansion using only small molecules of human neural progenitors for neurodegenerative disease modeling. PLoS One 8 (3), e59252. https://doi.org/10.1371/journal.pone.0059252.
Ren, Xuecong, Zhou, Hengda, Sun, Yujie, Fu, Hongying, Ran, Yu, Yang, Bing, et al., 2023. MIRO-1 interacts with VDAC-1 to regulate mitochondrial membrane potential in *Caenorhabditis elegans*. EMBO Rep. 24 (8), e56297. https://doi.org/10.15252/embr.202256297.
Roos, Jack, DiGregorio, Paul J., Yeromin, Andriy V., Ohlsen, Kari, Lioudyno, Maria, Zhang, Shenyuan, et al., 2005. STIM1, an essential and conserved component of store-operated Ca2+ channel function. J. Cell Biol. 169 (3), 435–445. https://doi.org/10.1083/jcb.200502019.
Sander, Paulina, Gudermann, Thomas, Schredelseker, Johann, 2021. A calcium guard in the outer membrane: is VDAC a regulated gatekeeper of mitochondrial calcium uptake? Int. J. Mol. Sci. 22 (2). https://doi.org/10.3390/ijms22020946.
Saotome, Masao, Safiulina, Dzhamilja, Szabadkai, György, Das, Sudipto, Fransson, Asa, Aspenstrom, Pontus, et al., 2008. Bidirectional Ca2+−dependent control of mitochondrial dynamics by the Miro GTPase. Proc. Natl. Acad. Sci. USA 105 (52), 20728–20733. https://doi.org/10.1073/pnas.0808953105.
Schindelin, Johannes, Arganda-Carreras, Ignacio, Frise, Erwin, Kaynig, Verena, Longair, Mark, Pietzsch, Tobias, et al., 2012. Fiji: an open-source platform for biological-image analysis. Nat. Methods 9 (7), 676–682. https://doi.org/10.1038/nmeth.2019.
Schwarz, Lisa, Fitzgerald, Julia C., 2022. Steady-state levels of Miro1 linked to phosphorylation at serine 156 and mitochondrial respiration in dopaminergic neurons. Cells 11 (8). https://doi.org/10.3390/cells11081269.
Schwarz, Lisa, Casadei, Nicolas, Fitzgerald, Julia C., 2021. Generation of R272Q, S156A and K572R RHOT1/Miro1 point mutations in iPSCs from a healthy individual using FACS-assisted CRISPR/Cas9 genome editing. Stem Cell Res. 55, 102469. https://doi.org/10.1016/j.scr.2021.102469.
Schwarz, Lisa, Sharma, Karan, Dodi, Lorenzo D., Rieder, Lara-Sophie, Fallier-Becker, Petra, Casadei, Nicolas, Fitzgerald, Julia C., 2022. Miro1 R272Q disrupts mitochondrial calcium handling and neurotransmitter uptake in dopaminergic neurons. Front. Mol. Neurosci. 15, 966209. https://doi.org/10.3389/fnmol.2022.966209.
Seo, Su Ryeon, Seo, Jeong Taeg, 2009. Calcium overload is essential for the acceleration of staurosporine-induced cell death following neuronal differentiation in PC12 cells. Exp. Mol. Med. 41 (4), 269–276. https://doi.org/10.3858/emm.2009.41.4.030.

Smolders, Stefanie, van Broeckhoven, Christine, 2020. Genetic perspective on the synergistic connection between vesicular transport, lysosomal and mitochondrial pathways associated with Parkinson's disease pathogenesis. Acta Neuropathol. Commun. 8 (1), 63. https://doi.org/10.1186/s40478-020-00935-4.

So, Edmund Cheung, Chow, Louis W.C., Chuang, Chin-Min, Chen, Cing Yu, Wu, Cheng-Hsun, Shiao, Lian-Ru, et al., 2025. MCU-i4, a mitochondrial Ca2+ uniporter modulator, induces breast cancer BT474 cell death by enhancing glycolysis, ATP production and reactive oxygen species (ROS) burst. Oncol. Res. 33 (2), 397–406. https://doi.org/10.32604/or.2024.052743.

Spillantini, M.G., Schmidt, M.L., Lee, V.M., Trojanowski, J.Q., Jakes, R., Goedert, M., 1997. Alpha-synuclein in Lewy bodies. Nature 388 (6645), 839–840. https://doi.org/10.1038/42166.

Stathopulos, Peter B., Schindl, Rainer, Fahrner, Marc, Zheng, Le, Gasmi-Seabrook, Geneviève M., Muik, Martin, et al., 2013. STIM1/Orai1 coiled-coil interplay in the regulation of store-operated calcium entry. Nat. Commun. 4, 2963. https://doi.org/10.1038/ncomms3963.

Valadas, Jorge S., Esposito, Giovanni, Vandekerkhove, Dirk, Miskiewicz, Katarzyna, Deaulmerie, Liesbeth, Raitano, Susanna, et al., 2018. ER lipid defects in neuropeptidergic neurons impair sleep patterns in Parkinson's disease. Neuron 98 (6), 1155–1169 e6. https://doi.org/10.1016/j.neuron.2018.05.022.

van Vliet, Alexander R., Jefferies, Harold B.J., Faull, Peter A., Chadwick, Jessica, Ibrahim, Fairouz, Skehel, Mark J., Tooze, Sharon A., 2024. Exploring the ATG9A interactome uncovers interaction with VPS13A. J. Cell Sci. 137 (4). https://doi.org/10.1242/jcs.261081.

Wang, Xinnan, Winter, Dominic, Ashrafi, Ghazaleh, Schlehe, Julia, Wong, Yao Liang, Selkoe, Dennis, et al., 2011. PINK1 and Parkin target Miro for phosphorylation and degradation to arrest mitochondrial motility. Cell 147 (4), 893–906. https://doi.org/10.1016/j.cell.2011.10.018.

Ying, W.L., Emerson, J., Clarke, M.J., Sanadi, D.R., 1991. Inhibition of mitochondrial calcium ion transport by an oxo-bridged dinuclear ruthenium ammine complex. Biochemistry 30 (20), 4949–4952. https://doi.org/10.1021/bi00234a016.

Zilka, Omkar, Shah, Ron, Li, Bo, Friedmann Angeli, José Pedro, Griesser, Markus, Conrad, Marcus, Pratt, Derek A., 2017. On the mechanism of cytoprotection by ferrostatin-1 and liproxstatin-1 and the role of lipid peroxidation in ferroptotic cell death. ACS Cent. Sci. 3 (3), 232–243. https://doi.org/10.1021/acscentsci.7b00028.

Zitt, Christof, Strauss, Bettina, Schwarz, Eva C., Spaeth, Nicola, Rast, Georg, Hatzelmann, Armin, Hoth, Markus, 2004. Potent inhibition of Ca2+ release-activated Ca2+ channels and T-lymphocyte activation by the pyrazole derivative BTP2. J. Biol. Chem. 279 (13), 12427–12437. https://doi.org/10.1074/jbc.M309297200.